FACULTÉ DES ÉTUDES SUPÉRIEURES ET POSTOCTORALES

uOttawa

L'Université canadienne
Canada's university

FACULTY OF GRADUATE AND POSDOCTORAL STUDIES

Marina Gertsvolf
AUTEUR DE LA THÈSE / AUTHOR OF THESIS

Ph.D. (Physics)
GRADE / DEGREE

Department of Physics)
FACULTÉ, ÉCOLE, DÉPARTEMENT / FACULTY, SCHOOL, DEPARTMENT

Controlled Material Modification of Transparent Dielectrics by Femtosecond Laser Pulses
TITRE DE LA THÈSE / TITLE OF THESIS

Paul Corkum
DIRECTEUR (DIRECTRICE) DE LA THÈSE / THESIS SUPERVISOR

CO-DIRECTEUR (CO-DIRECTRICE) DE LA THÈSE / THESIS CO-SUPERVISOR

EXAMINATEURS (EXAMINATRICES) DE LA THÈSE / THESIS EXAMINERS

Xiaoyi Bao

Stephen Mihailov

Réeal Vallée (Université de Laval)

Tong Xu

Gary W. Slater
Le Doyen de la Faculté des études supérieures et postdoctorales / Dean of the Faculty of Graduate and Postdoctoral Studies

CONTROLLED MATERIAL MODIFICATION OF TRANSPARENT DIELECTRICS BY FEMTOSECOND LASER PULSES

Marina Gertsvolf

Thesis submitted to the
Faculty of Graduate and Postdoctoral Studies
In Partial Fulfillment of the Requirements
For the Degree Doctor of Philosophy in Physics

Department of Physics
Faculty of Science
University of Ottawa

Library and Archives
Canada

Published Heritage
Branch

395 Wellington Street
Ottawa ON K1A 0N4
Canada

Bibliothèque et
Archives Canada

Direction du
Patrimoine de l'édition

395, rue Wellington
Ottawa ON K1A 0N4
Canada

Your file Votre référence
ISBN: 978-0-494-61231-6
Our file Notre référence
ISBN: 978-0-494-61231-6

NOTICE:

The author has granted a non-exclusive license allowing Library and Archives Canada to reproduce, publish, archive, preserve, conserve, communicate to the public by telecommunication or on the Internet, loan, distribute and sell theses worldwide, for commercial or non-commercial purposes, in microform, paper, electronic and/or any other formats.

The author retains copyright ownership and moral rights in this thesis. Neither the thesis nor substantial extracts from it may be printed or otherwise reproduced without the author's permission.

AVIS:

L'auteur a accordé une licence non exclusive permettant à la Bibliothèque et Archives Canada de reproduire, publier, archiver, sauvegarder, conserver, transmettre au public par télécommunication ou par l'Internet, prêter, distribuer et vendre des thèses partout dans le monde, à des fins commerciales ou autres, sur support microforme, papier, électronique et/ou autres formats.

L'auteur conserve la propriété du droit d'auteur et des droits moraux qui protège cette thèse. Ni la thèse ni des extraits substantiels de celle-ci ne doivent être imprimés ou autrement reproduits sans son autorisation.

In compliance with the Canadian Privacy Act some supporting forms may have been removed from this thesis.

While these forms may be included in the document page count, their removal does not represent any loss of content from the thesis.

Conformément à la loi canadienne sur la protection de la vie privée, quelques formulaires secondaires ont été enlevés de cette thèse.

Bien que ces formulaires aient inclus dans la pagination, il n'y aura aucun contenu manquant.

Canada

Abstract

Wide band gap dielectrics remain transparent for low intensity near-infrared light. However, when light intensity increases, highly nonlinear absorption takes place. The absorption occurs due to the transfer of electrons from the valence to the conduction band in the dielectric. We investigate the physics of this ionization process and the material changes induced in the sample by multiple femtosecond laser pulses.

We show how transmission relates to the ionization probability in high density material. By controlling various experimental parameters we obtain qualitatative and quantitatative information about ionization and different mechanisms involved.

Analyzing transmission for a variety of pulse durations, we obtain the field dependent collisional ionization rates for fused silica.

Using elliptically polarized light, we probe the sub-laser-cycle dynamics of the ionization. The variation in the ionization rate within a laser cycle is translated, through the differential absorption between the major and the minor axes of the polarization ellipse, into the polarization changes of the transmitted light.

In crystalline samples we observe a dependence of the ionization on the alignment of the field with the lattice. The modulation in transmission with the alignment angle of the crystal is analyzed using Fourier transformation and it provides the information on the lattice symmetry. We find that the directionally dependent electron effective mass plays an exponentially dominant role in defining the ionization probabilities.

Chemical changes inside the focal volume accumulate over many laser shots. We show that these material changes lead to a localized increase in the ionization, providing a feedback mechanism that leads to the formation of nano-structures in the interaction region.

With longer exposure time, defocusing micro-lenses are formed in the bulk. These micro-lenses change the divergence of the laser beam as well as the pulse energy required for the ionization, therefore, leading to enhanced transmission. We observe this effect in a variety of transparent dielectrics.

In crystalline quartz we find a novel phenomenon associated with repeated ionization. The permanent changes in the sample create favourable phase matching conditions for strong second harmonic generation.

Publications

CHAPTER	PUBLICATION
2	"Transient nanoplasmonics inside dielectrics" P.P. Rajeev, M. Gertsvolf, C. Hnatovsky, E. Simova, R. S. Taylor, P.B. Corkum, D.M. Rayner and V.R. Bhardwaj, J. Phys. B., B/239809/SPE, (2007) "Field Dependent Avalanche Ionization Rates in Dielectrics" P. P. Rajeev, M. Gertsvolf, P. B. Corkum, and D. M. Rayner, Phys. Rev. Lett. 102, 083001 (2009)
3	"Attosecond Ionization Dynamics Inside Transparent Solids" M. Gertsvolf, M. Spanner, D. M. Rayner and P. B. Corkum, Phys. Rev. Lett. submitted
4	"Orientation-Dependent Multiphoton Ionization in Wide Band Gap Crystals" M. Gertsvolf, H. Jean-Ruel, P. P. Rajeev, D. Klug, D. M. Rayner and P. B. Corkum, Phys. Rev. Lett. 101, 243001 (2008)
5	"Memory in Nonlinear Ionization Of Transparent Solids" P. P. Rajeev, M. Gertsvolf, E. Simova, C. Hnatovsky, R. S. Taylor, V. R. Bhardwaj, D. M. Rayner, P. B. Corkum, Phys. Rev. Lett. 97, 253001 (2006) "Self-controlled formation of micro-lenses by optical breakdown inside wide-band-gap materials" D. Grojo, M. Gertsvolf, H. Jean-Ruel, S. Lei, L. Ramunno, D. M. Rayner, and P. B. Corkum, Appl. Phys. Lett. 93, 243118 (2008)

Contents

List of Figures

Chapter 1

Introduction

Transparent dielectrics are an ideal media for building integrated electro-optical components, 3-dimensional photonic circuits and microfluidic devices [1, 2]. The wide band gap of such materials guarantees low absorption and dispersion for visible and infrared light, the spectral range where microscopy and optical communications occur.

Until recently, UV light combined with etching was used to create these devices. Resonant absorption of UV photons by dielectric material causes the modification of its molecular structure. As a result the refractive index and the absorption properties are modified as well as the etching rate [3]. This allows the construction of such optical devises as frequency selective optical waveguides and microfluidic channels.

The growing simplicity and flexibility of femtosecond laser sources allows off-resonant multi-photon absorption to replace the UV illumination for some applications [4]. Multi-photon absorption causes ionization by transferring the electrons in the material from the top of a valence band to a conduction band. For a typical dielectric material such as fused silica with a band gap of 9 eV and a standard 800 nm Ti:Sapphire femtosecond laser, each ionization event requires the absorption of 6 photons. This high order multi-photon process is extremely intensity dependent and provides an excellent spatial control of the modification area. Multi-photon absorption can be localized inside a 3-dimensional volume providing another advantage over UV light. This can drastically improve the capabilities of optical device manufacturing and has a great technological importance.

The study of interaction of intense light pulses inside the solid is difficult since there are only few diagnostic tools at the disposal of experimental researchers. The experimental tools developed for the studies of strong field interactions in atoms and molecules are not applicable in solids. High harmonic generation (HHG) spectroscopy, attosecond extreme ultraviolet (XUV) streaking or ion and electron imaging [5] are not accessible. Novel approaches are required for the studies of dielectrics interaction with femtosecond laser radiation. We have developed methodology specifically for solids. Unlike on surfaces or in isolated atoms and molecules, in the bulk there is no direct access to the electrons and ions created by the ionization. Light transmitted through the dielectric material is the only measurable quantity. The spatial and structural changes due to ionization can be analyzed post-interaction using imaging microscopy [6]. The real-time measurements are limited to the analysis of the transmitted light properties such as absorption or polarization [7]. The changes in the transmitted signal are integrated over the interaction volume, making the analysis more complicated. They can be used to gain information on the pulse-to-pulse dynamics of the interaction.

The fundamental physical aspects of the interaction process are not yet fully understood. Theoretical studies are equally challenging as (i) many body quantum calculations have to be implemented that can account for the large number of atoms presents in the interaction volume, (ii) perturbation theory can no longer be used due to the high intensities involved, (iii) nonlinear optical and plasma effects have to be included to account for light propagation, and (iv) several physical processes describing the ionization have to be incorporated. State of the art calculations can currently deal with up to 10^6 atoms cm^{-3}, when the solid densities are 10^{22} atoms cm^{-3}.

We start by comparing the transparent dielectrics with gases. In transparent solids the band gap is comparable to the ionization potential of molecules; hence, band to band transition in solids is equivalent to ionization in atoms and the dynamics of the ionization process should also be similar. Indeed the fundamental theoretical work on ionization by strong fields [8] describes both media in similar terms.

One important difference between molecules and solids is the density of the material. In solids the number of atoms in the interaction region exceeds the number of photons and, therefore, the number of photo-electrons produced by the laser pulse many times [1]. This results in strong laser absorption and high ionization efficiency.

We focus the laser beam inside the bulk. Using microscope objective with high numerical aperture we can reach the intensities required for multiphoton ionization without exceeding the power threshold for self-focusing. This tight focusing also eliminates surface effects and confines the interaction to the true 3-dimensional case. When the intensity of the focused laser beam

---

[1] 800 nm, 50 nJ laser pulse focused to $30\mu m^3$ volume, gives the photon density $N_{\hbar\omega} = 0.7 \times 10^{22}$ cm^{-3}. The molecular number density of fused silica $N_a = 2.2 \times 10^{22}$ cm^{-3}. For 6 photon absorption the maximum possible density of carriers, $N_e = N_{\hbar\omega}/6 = 0.1 \times 10^{22}$ cm^{-3}, hence, $N_a > 18 \times N_e$.

reaches the level sufficient for the multi-photon ionization, absorption occurs with almost 100% probability due to the high density of the material. As a result the laser pulse gets depleted and the intensity across the focal volume is clamped [7, 9]. We can approximate absorption by a threshold function. We call this process "lawn-mower" absorption because it resembles cutting the grass. The grass level does not exceed the blade height anywhere across the lawn (Fig. 1.1).

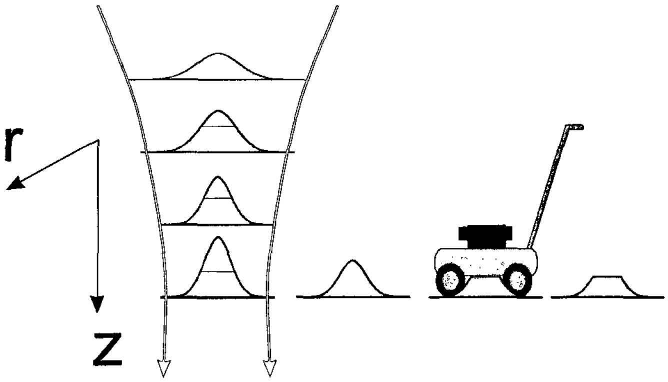

Figure 1.1: Lawn-mower absorption. Similar to grass clipping the laser pulse intensity is clamped along the focus due to absorption.

Intensity clamping self-limits the modification of the material. By increasing the laser intensity or its power we increase the volume for multi-photon absorption, without changing the deposited energy density significantly. Therefore, material modification has high tolerance to the experimental conditions such as laser pulse duration and power stability. This provides a great gain for technological applications. Laser pulse depletion translates into strong absorption and can be easily measured experimentally. The intensity clamping level depends on the band gap of the dielectric.

In fact, the analysis of the transmitted laser radiation is the only readily available tool for studies of multi-photon ionization inside solids. The "lawn-mower" model neglects propagation effects due to pulse depletion but provides excellent insight into the multi-photon ionization and absorption inside solids.

The "lawn-mower" does not describe accurately the evolution of the absorption during the laser pulse, when collisional ionization (avalanche) grows. It treats all absorption mechanisms together using single intensity threshold. In order to model the nonlinear ionization better, we solve the electron density rate equation: $dn/dt = W(I) + \beta n$. The model parameters such as multi-photon ionization rate, $W(I)$, and avalanche rate β can be obtained from fitting to the experimental data. The relative importance of the two processes and their dependence on the conditions of the experiment such as pulse duration, provide an important insight into the physics of ionization.

In our experiments we focus laser pulses inside the transparent sample and collect the transmitted radiation. We have several control parameters: laser pulse energy, its duration and polarization state. For detection we can measure the total transmitted light, fully characterize its polarization state and analyze its spectrum. We will show how we use the transmission measurements to study ionization mechanisms and their spatial and dynamical properties.

Our experiments are very much influenced by what we are learning in atomic and molecular ionization. Although in solids we make a band to band transition, the ideas are otherwise similar.

- In atomic and molecular ionization, the electron driven by the laser electric field can collide with the parent ion. Atomic experiments show that even with low energy recollision electrons (i.e. low intensity light), the inelastic scattering is very effective because the field lowers the Coulomb barrier [10]. The resulting non-sequential double ionization is equivalent to avalanche in solids, except in solids the collisions are not restricted to the parent ion. We should expect low energy collisions to also effect avalanche in solids – with the laser field again playing an important role.

We call these processes cold avalanche [11] because they grow with the number of free carriers and involve kinetically-cold electrons and ions. These processes have never been observed before in solids. We will show that we have the tools to measure multi-photon and avalanche rates. Due to the different intensity dependence of the two mechanisms, our results show that effective avalanche ionization rate β changes with pulse duration. The increase in β for shorter pulses provides direct evidence of cold avalanche.

- Based on experiments in atoms and molecules we expect the multi-photon ionization in solids to have a sub-laser-cycle dynamics. For a linearly polarized laser field, the ionization would be the strongest at the peak of the cycle. Due to the pulse depletion we expect the sub-cycle absorption to reshape the laser electric field. An avalanche, on the other hand, is un-phased with the laser field and depends only on the pulse envelope.

We can extend our transmission experiments to measure the sub-cycle reshaping of the laser electric field caused by direct multi-photon ionization. In our experiment [12, 13] we used elliptically polarized laser pulses. The sub-cycle variations in the multi-photon ionization rate lead to the differential absorption between the major and the minor axes of the polarization ellipse. As a result the polarization state of the transmitted light is modified. We find that, for short pulses, the changes in the polarization state were the strongest.

- In molecules the tunneling probability strongly depends on the alignment angle between the laser polarization and the molecular axis [14]. The reasons are multi-fold and can differ in importance from molecule to molecule. They include free electron wave-packet interference [15, 16], core electrons contributions [17] and molecular polarizability [18]. In solids, the lattice symmetries should similarly affect the ionization rates. We employ ionization metrology to study the origin of spatial modulation in the ionization of crystals. Our results are consistent, in quartz, with the variation in the electron effective mass as a function of the angle, with respect to the crystal axis, producing a modulation of the multi-photon ionization rates. This μm^3 and fs resolution in the measurements of crystal symmetry adds a novel powerful microscopy tool.

- So far we have ignored chemistry. However, repeated ionization of the same focal volume with multiple laser pulses causes chemical changes in the material that accumulate. These changes can modify the band gap. This can be directly detected through absorption measurements [19]. Repeated ionization of the focal volume by millions of laser shots induces macroscopic changes in the material that affect laser focusing [20] and are accompanied by the reduction in the nonlinear absorption.

These changes have consequences for photonics. We found that the creation of the defocusing micro-lens in the interaction region was present in all dielectrics we have studied. This provides a novel way of building 3-dimensional photonic devices. For fused silica due to the periodic structure of the modification, polarization selective photonic components can be built.

In crystal quartz the modification of the material in the focal region is preceded by strong enhancement of the spontaneous second harmonic (SH) generation. This SH memory provides a sensitive tool to study the orientation dependent multi-photon ionization in quartz and also a potentially highly efficient source for wavelength conversion.

In conclusion, dielectrics are the basis material for photonics just as the semiconductors are for electronics. However the technological and the fundamental developments of photonics are far behind. Intense femtosecond lasers promise a unique tool for studying and modifying the dielectrics. We have developed highly sensitive methods for studying strong field ionization, measuring the material properties of transparent solids, based of laser depletion and modifying the material in a controlled manner.

Chapter 2

Ionization Metrology Through Depletion

In this chapter we will present the experimental and the theoretical treatment of the nonlinear absorption of tightly focused low power femtosecond laser pulses inside transparent dielectrics. The ionization process is dominated by laser intensity depletion due to the high density of solids. Our theory predicts the injected electron density in the focal volume for different regimes of the laser pulse energy and duration. We will show how by varying laser parameters we probe different ionization mechanisms, such as direct multi-photon ionization and avalanche. The high sensitivity of our measurements allows access to field dependent collisional ionization rates.

The basic theoretical model that describes the strong field ionization both in gas phase atoms and solids was first presented by Keldysh in 1965 [8]. Since then it has been extended and improved significantly to describe the ionization of gas phase atoms and molecules [21, 22] and the consequences for strong field processes such as enhanced ionization [23], re-collision and the generation of high harmonics [24] among others. Progress has come through comparison with the detailed experiments in the gas phase where the electron and ion yields and momenta are measured as well as the high harmonic spectroscopy.

Similar progress has not followed in solids. Keldysh's 1965 paper remains, to this day, the basis for including the strong field ionization in discussions of laser material interaction. Electrons, ions and high harmonics emission are confined and cannot be accessed from the outside. The lack of experimental tools for the studies of multi-photon ionization in dielectrics has delayed the development of the theoretical models.

Most of the fundamental research in solids is based on the studies of the surface damage threshold [25]. In addition, measurements have used interferometric techniques to evaluate the electron density in the focal volume [26, 27]. Phenomenologically most studies are aimed at applications for laser machining and dielectrics modification.

We will describe an approach to study the ionization process more directly. We will show how the transmission as a function of the laser pulse parameters can reveal the fundamentals of the ionization process. We expand a simple analytical description [7] and give details of the approach that has led the concept of "nonlinear memory" [19], ionization in crystals [28], field assisted avalanche [29] and others.

In the gas phase the density of the sample is negligible compared to the photon flux. In contrast, in solids, the situation is reversed. For example, the photon flux density, $N_{\hbar\omega}$ of 50 nJ, 800 nm laser pulse focused inside 30 μm^3 volume is only 0.7×10^{22} cm^{-3}, whereas the solid molecular density (*e.g.* fused silica), $N_a = 2.2 \times 10^{22}$ cm^{-3}. If laser pulse energy were fully depleted due to ionization in a 9 eV band gap dielectric, the resulting carrier density would have reached 0.1×10^{22} cm^{-3}, effectively ionizing less than 5% of the molecules. The low ratio of photons compared to the atomic density,

$$r_n = N_{\hbar\omega}/N_a \ll 1, \tag{2.1}$$

leads to strong laser absorption. The absorption plays a central role in controlling the laser material interaction. Experimentally the absorption can be used to probe the ionization process inside solids.

Generally the energy from the femtosecond laser pulse is transferred to the material via the generation of carriers and scattering. In wide band gap dielectrics and with sufficiently short pulses, multi-photon ionization is the dominant mechanism that injects carriers into the conduction band. Conduction band electrons gain kinetic energy through inverse Bremsstrahlung scattering. Conventionally it is assumed that when their energy exceeds the band gap, Δ, impact ionization can occur, leading to avalanche. Effectively, the absorbed energy density, E_A, is defined by the generation of the carrier density, n that occurs during the femtosecond pulse as shown in Eq. (2.2). Each electron "costs" the laser pulse one band gap of energy.

$$E_A = \Delta \times n. \tag{2.2}$$

The theoretical models that describe electron density in the conduction band usually account for the following processes: multi-photon ionization, avalanche, electron recombination and trapping [30]. The complete description of the ionization inside bulk should be based on the solution of the wave equation for the laser field. It should include the focusing by microscope objective (including aberrations) nonlinear polarization effects, dispersion, absorption (multi-photon, scattering, traps liberation), plasma dispersion and refraction. It is a numerically challenging exercise where it is hard to singe out any specific contribution. Hence the essential physics is masked.

There are several research papers that describe many of these contributions in the analysis of the dielectrics breakdown [9, 31]. Our analysis is based on the reduced approach designed to apply under such experimental conditions where low order nonlinear polarization, refraction and plasma effects can be neglected.

In our theoretical model we assume Gaussian focusing to describe the intensity increase inside the sample and we account for several ionization mechanisms that lead to carrier generation and absorption, such as strong field ionization, avalanche and photon assisted collisional ionization.

We show that our methodology for the study of the multi-photon ionization through absorption can be applied to high density gases. Here we use well established ionization rates for atoms to model absorption as a function of the input laser pulse energy. We can accurately predict absorption for pulse lengths varying between few femtoseconds to picoseconds. These results confirm that we have built a general method to study ionization by femtosecond laser pulses through absorption.

2.1 Experimental setup

Our experimental setup is built to allow transmission measurements through dielectric materials. We control several critical experimental parameters such as pulse duration, energy, repetition rate and polarization.

In our experiments we use 800 nm 40 fs and longer laser pulses, focused inside transparent 1 mm thick fused silica slab with microscope objective (numerical aperture, NA = 0.25). The focus is located 150 μm inside the sample to avoid aberrations. The tight focusing geometry allows us to reach high intensities, well inside the sample. In this way we eliminate surface effects and guarantee a fully 3-dimensional interaction.

We use low $F_{\#}$ to prevent the influence of low order nonlinear effects on propagation. We can reach intensities required for material breakdown, while keeping the peak power below the critical level for self-focusing or self-phase modulation. (*e.g.* P_C(fused SiO_2) = 2.6 MW).

The laser system consists of "KMLabs" femtosecond oscillator, in-house built grating-based pulse stretcher, "Coherent RegA" regenerative amplifier and in-house built grating-based pulse compressor. We control the pulse duration by applying quadratic chirp when changing the grating – mirror separation in the compressor. We can change the pulse duration between 40 fs and 1.5 ps.

The repetition rate of the laser is controlled through the external triggering of the RegA cavity Q-switch. The trigger signal is provided by the "Master Clock" and can be varied between single pulse bursts and up to the kHz range.

The laser beam at the output of the pulse compressor is spatially filtered using a telescope with a pinhole. This also allows to increase the beam spot size. The laser system supplies up to 4.5 μJ pulse energy.

The system schematics are presented in Fig. 2.1. The input pulse energy at the sample is controlled by a half-wave-plate (HWP_1) – polarizer (PBS_1) combination. The polarization state of the incident light is controlled by a quarter-wave-plate (QWP_1) and a HWP_2 combination that allows independent control over laser ellipticity and major axis orientation. The transmitted light is collected alternatively by an integrating sphere or a collimating objective. When collimated, the transmitted light polarization state is analyzed by a rotating polarizer (PBS_2).

For different experiments we can mount any HWP or PBS on computer controlled rotation stages. The sample is also mounted on two-axis translation stage to allow it to move to a fresh spot between laser shots if needed.

We use a microscope objective (numerical aperture NA = 0.25, $F_{\#}$ = 0.13) to focus the laser beam inside the sample. If the focus were in vacuum, the peak intensity would be of the order 10^{14} W cm^{-2}.

To ensure tight focusing, the size of the laser beam incident on the microscope objective exceeds its clear aperture. This results in a flat top spatial profile in the far field.

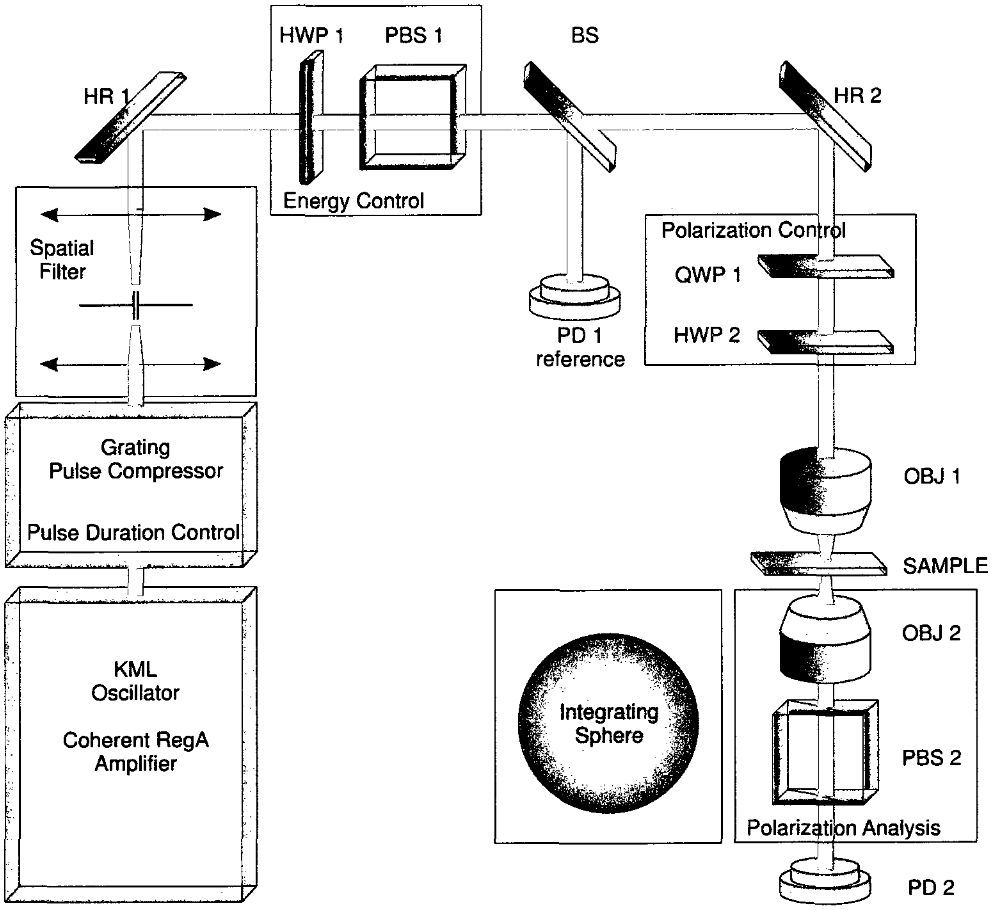

Figure 2.1: Experimental setup schematics. HR - high reflector, BS - beam splitter, QWP - quarter-wave-plate, HWP - half-wave-plate, PBS - polarizer, OBJ - microscope objective, PD - photo-diode.

2.2 Laser propagation and Electron densities

The full wave equation that describes laser pulse propagation inside the sample consists of multiple terms. Taking into account the slowly varying amplitude approximation, it takes the form shown in Eq. (2.3).

$$\frac{d\bar{E}}{dz} = (\hat{D} + \hat{N})\bar{E}, \tag{2.3}$$

where $\bar{E}$ is the electric field. $\hat{D}$ describes laser propagation including dispersion, refraction, Kerr effects and plasma refraction effects. $\hat{N}$ represents the laser absorption through carrier generation. We use a split-step methodology in numerical calculations to separate between $\hat{D}$ and $\hat{N}$. we will show that under our experimental conditions, $\hat{D}$ is reduced to Gaussian beam focusing.

The absorption of the laser electric field, $\hat{N}\bar{E}$ is directly related to the carrier density. The rate of absorbed energy density dE_A/dt in a unit volume of area dS and depth dz is equivalent to the change in laser intensity dI/dz. For the band gap, Δ, the Eq. (2.2) takes the form (2.4), we will use it to describe $\hat{N}\bar{E}$.

$$\frac{dI}{dz} = \Delta \frac{dn}{dt}. \tag{2.4}$$

The standard, commonly used [25], electron density rate equation for the conduction band in dielectrics takes the form presented in Eq. (2.5):

$$\frac{dn}{dt} = W(I) + n\beta(I). \tag{2.5}$$

Here $W(I)$ is the multi-photon ionization rate, describing the injection rate of electrons into the conduction band by intense laser field. The formalism for $W(I)$ is introduced in [8] but as we will show later it can also be approximated by a step function.

The $n\beta(I)$ part describes electron injection by impact ionization and therefore depends on the number of carriers, n in the conduction band. The $\beta(I)$ is the impact ionization rate and in its simplest form, $\beta = \alpha_0 I$, accounts for the electron heating through inverse Bremsstrahlung scattering. We will show later that in the presence of the strong laser field impact ionization rate can be modified by the presence of the field and take the form $\beta(I) = \sum \alpha_j I^j$ [29].

The $\beta(I) = \alpha_0 I$ approximation is in good agreement with the result of the full kinetic model developed for conduction electrons by [32]. The same linear dependence of β on laser intensity arises from the flux doubling model as shown in [32].

Critical inspection of Eq. (2.5) reveals that it neglects electron trapping mechanisms. For the electron – ion recombination the characteristic time, $\tau_{rec} \approx 1$ ps for dielectrics [26]. This τ_{rec} is much longer than the pulse duration and the approximation to exclude it from Eq. (2.5) is well justified. In the materials where exitons are allowed (*e.g* SiO_2) and τ_{rec} is known to be short [26], trapping should be included in Eq. (2.5) at first sight. However, initially populated free exiton states, located just under the conduction band [33], immediately release electrons into the conduction band in the presence of the strong laser field. The release rate exceeds both the $W(I)$ and the $\beta(I)$ and, therefore, trapping can be neglected in Eq. (2.5).

From Eq. (2.4) and (2.5) we obtain Eq. (2.6) to use in propagation calculations:

$$\frac{dI}{dz} = \Delta \left\{ W(I) + n\beta(I) \right\}. \tag{2.6}$$

Here we have implicitly used the assumption from the flux doubling model, that no kinetic energy is left in the electrons following the impact ionization. In principle additional kinetic energy left in the electrons, ϵ, can be accounted for in Eq. (2.6) if we write

$$\frac{dI}{dz} = \Delta \left\{ W(I) + \left(1 + \frac{\epsilon}{\Delta}\right) n\beta(I) \right\}. \tag{2.7}$$

We have estimated from our numerical modeling that the maximum change in the electron density due to $\epsilon \approx 0.5\Delta$, is only of the order of 2 and therefore can be neglected.

Integrating over the pulse duration and propagation length Eq. (2.5) and Eq. (2.6) we predict the electron density distribution inside the interaction region. For example, our calculations show that under wide range of experimental conditions, the electron density remains uniform inside the focal volume. This uniformity helps to explain why the formation of nano-structures inside fused silica demonstrates high tolerance to the laser pulse energy and duration [34].

Rather than fully solving Eq. (2.3), we now introduce a model that is intuitive, yet captures the essential features of the multi-photon ionization.

2.3 "Lawn-mower"

The probability of ionization in atoms and molecules with ionization potential IP depends exponentially on the ratio between the photon energy, $\hbar\omega$, the $N_{\hbar\omega}$ and the IP. In dielectrics the band gap Δ plays the role of IP [8]. For transparent dielectrics, with band gap exceeding the photon energy by several times, the multi-photon probability increase with the laser field strength is highly nonlinear. Combined with $r_n \ll 1$ (Eq. (2.1)) this results in the threshold-like ionization probability. For low laser intensity the ionization probability is close to zero. For the laser intensity above a certain threshold value, I_{th}, the probability increases sharply. The I_{th} is related to the ionization rate as we will show later.

Using threshold - like absorption we can write an analytical model for the depletion of a laser beam, assuming a Gaussian focusing geometry. This model has been first presented in Ref. [7]. It is based on the assumption that the laser pulse intensity is clamped when, due to focusing, it exceeds the threshold level I_{th}. Neglecting avalanche ionization, we assume that the I_{th} remains unchanged through the pulse. Assuming that the focusing geometry does not change due to intensity clamping, the analytical formula (Eq. (2.8)) can be derived to describe laser absorption.

$$A = \mathrm{erf}\left(\sqrt{\mathrm{X}}\right) - \frac{2}{\sqrt{\pi}}\mathrm{e}^{\mathrm{X}}\left(1+\frac{2}{3}\mathrm{X}\right)\sqrt{\mathrm{X}}, \tag{2.8}$$

where $X = \ln(I/I_{th})$, I is the peak intensity if the focus were in vacuum.

It is interesting to note that transmission depends only on one parameter, I/I_{th}. This simple analytical form provides a good insight when comparing experimental results for different focusing geometries, corresponding to different I, or materials with different band gaps, corresponding to different I_{th}.

In Fig. 2.2 we see the experimental and theoretical transmission curves for fused SiO_2. Using $I_{th} = 1.2 \times 10^{13}$ W cm^{-2} the model agrees well with experiment around the breakdown threshold region. At higher input pulse energies the deviation of the model from the experiment is due to the contribution of inverse Bremsstrahlung and avalanche. These result in stronger absorption, which is not built into the "lawn-mower" model.

One major result of this model is the intensity clamping through the interaction region. This is an important feature that allows strong increase in the incident pulse energy without the increase in the low order nonlinear effects. Intensity clamping results in uniform carrier density in the interaction region. The analytical solution for the spatial distribution of the carrier

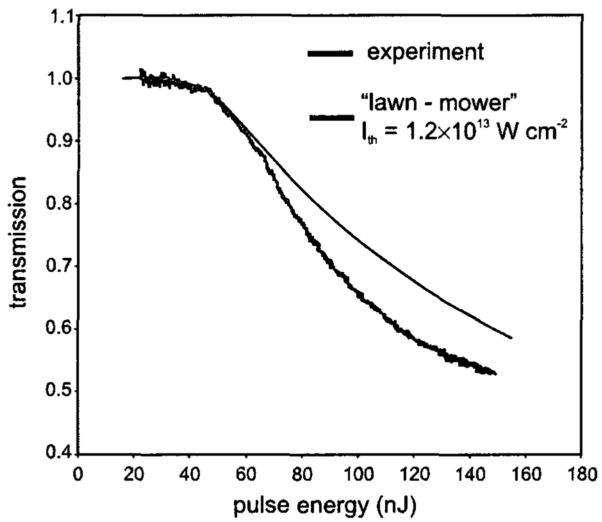

Figure 2.2: Transmission as a function of the input pulse energy. Solid blue – experimental results for 800 nm 45 fs laser pulses focused (NA = 0.25) through a fused silica slab (Suprasil I). Dashed red – "lawn-mower" model with $I_{th} = 1.2 \times 10^{13}$ W cm^{-2}.

density injected in the interaction region (equal to the absorbed laser energy density divided by Δ) has the form shown in Eq. (2.9).

$$N(z,r) = \frac{-4I_{th}\tau\,(Y-1)}{\Delta z Y}\sqrt{\ln\left(\frac{I/I_{th}}{Y}\right) - \frac{r^2/\omega_0^2}{Y}}, \tag{2.9}$$

where $Y = (1 + z^2/z_0^2)$, τ ic the pulse length, ω_0 and z_0 are the waist size and the Rayleigh length respectively. Integration of this expression over z and r leads to the same result for A as Eq. (2.8), as expected.

In order to correlate I_{th} with ionization rates, we use numerical models that are similar in approach to the analytical "lawn-mower". That is, we assume that pulse propagation is unchanged, only the intensity structure of the beam is modified. We model the carrier density generation rate, dn_e/dt as the laser pulse propagates through the focus. We use Eq. (2.5) and Eq. (2.6) to model laser depletion and carrier density generation. Since we are focusing in our analysis on the absorption near the threshold and for shorter laser pulses, we assume that $\beta = 0$. The result of this numerical modeling is equivalent to the analytical solution (2.8) when ionization rate, $W(I)$, is approximated with a step function as in Eq. (2.10).

$$W(I) = \begin{cases} 0, & I < I_{th} \\ \infty, & I \geq I_{th} \end{cases} \tag{2.10}$$

Having the numerical modeling tool available, we can extend the analysis of carrier injection to account for another ionization mechanism present in solids – impact ionization or avalanche. The analytical "lawn-mower" model can not account for the avalanche contribution in absorption. Consequently, the experimental results start deviating from the theory when the laser pulse length increases. We will show later that by including the avalanche coefficient, $\beta(I)$, in numerical models we achieve good agreement between the theory and the experiment for a wide range of pulse durations and laser input pulse energies.

Before continuing, it is important to address several issues concerned with the beam refraction. It is the basic assumption of our theory that laser propagation remains unchanged (except for clamping) for a wide range of input pulse energies.

Generally the beam propagation should include dispersion, nonlinear refraction, beam focusing by the microscope objective, and plasma refraction. The pulse broadening due to dispersion ($\beta_2 = 36$ fs^{2}mm^{-1} for fused SiO$_2$) is negligible for 30 nm pulse bandwidth and ~20 μm interaction length.

In the range of the pulse energies that are below the breakdown threshold, the pulse power remains below the critical power for self-focusing ($P_C \approx 2.6$ MW in fused silica, or 115 nJ for 45 fs pulse). In the range of higher pulse energies, the peak power is clamped inside the material due to pulse depletion long before the focal region. This is confirmed by the absence of self-phase modulation in the transmitted spectrum [7]. As a result, we can neglect the impact of all low order nonlinear effects such as Kerr effects and Raman scattering [35] on the beam propagation.

We minimize the spherical aberration effect by keeping the focal point close to the surface of the sample (150 μm below the surface for NA = 0.25 objective).

For longer pulses and higher pulse energies, avalanche ionization can increase the plasma density, leading to plasma refraction. The plasma refraction results in the defocussing of the laser beam. Experimentally this translates into absorption saturation at higher pulse energies. Our self-limiting propagation model does not take plasma effects into account. Therefore, we limit the analysis of the transmission results to the region around the breakdown threshold energies.

The self limiting absorption model is an ad hoc treatment of the beam propagation and absorption. However, it provides an excellent qualitative and quantitative description of multi-photon absorption in solid. We verify the "lawn-mower" model by solving the 2-dimensional time dependent

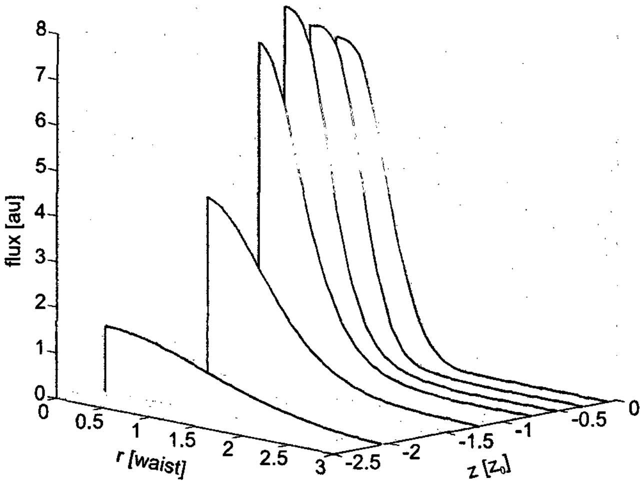

Figure 2.3: Radial intensity distribution along the propagation axis. Input pulse energy 60 nJ, which corresponds to the intensity of 1.5×10^{13} W cm^{-2}, if the focus were in vacuum.

Helmholtz wave equation (Eq. (2.11)) [35] numerically.

$$\frac{\partial^2 \tilde{E}}{\partial z^2} + \nabla_T^2 \tilde{E} = -\left(\frac{n\omega}{c}\right)^2 \frac{\partial^2 \tilde{E}}{\partial t^2}. \tag{2.11}$$

Here we have used the approximation that the refractive index of material, n, varies slowly in space and time. $\tilde{E}$ is the laser electric field and ∇_T^2 is the tangential part of the Laplace operator. Applying scalar paraxial approximation with cylindrical symmetry, we obtain the equation for the field envelope, E (2.12).

$$\frac{\partial E}{\partial z} = -\frac{ic}{2\omega n}\nabla_T^2 E + \frac{n}{c}\frac{\partial E}{\partial t}. \tag{2.12}$$

The absorption and refraction due to plasma generation and self-focusing are introduced through the complex refractive index (2.13)

$$n = (n_0 + n_2 I)\sqrt{1 - \frac{N_e}{n_0^2 N_c}} + i\frac{W_I \Delta}{2I}, \tag{2.13}$$

where I is the laser intensity, n_0 and n_2 are the material refractive index and nonlinear coefficient, N_e and N_c are the injected and the critical electron densities. W_I is the ionization probability (multi photon and avalanche) and Δ is the material band gap.

In Fig. 2.3 we show the radial distribution of laser pulse fluence along the propagation axis for the input pulse energy 60 nJ. The radial profile changes from Gaussian to flat – top at the onset of absorption at $z \approx -0.5z_0$, in agreement with the limiting absorption model.

The intensity and the electron density clamping obtained by numerical modeling agree with the results of the "lawn-mower" predictions.

2.4 Multi-photon ionization rates

The ionization of wide band gap dielectrics with femtosecond laser pulses is similar to the case of atoms. In atoms two regimes of ionization, tunneling and multi-photon are defined for intense laser field. They are separated in the analytical theories by Keldysh's γ parameter [8]. This parameter depends on the laser frequency, ω, atomic ionization potential, IP, and the field strength, E, that can be related to the photon flux density, $N_{\hbar\omega}$.

$$\gamma = \omega\sqrt{2mIP}/eE \tag{2.14}$$

In solids, the ionization potential, IP, is replaced by band gap, Δ and Eq. (2.14) takes the form:

$$\gamma = \omega\sqrt{m\Delta}/eE, \tag{2.15}$$

where m now is the reduced mass of electron and hole.

For $\gamma \ll 1$, the ionization is in tunneling regime, for $\gamma \gg 1$, the ionization is multi-photon. Tunneling ionization is characterized by sub-laser-cycle dynamics, whereas multi-photon depends on the pulse intensity envelope.

In the same paper Keldysh has described the two regimes in the ionization of solids [8]. He presented the complete solution to the ionization rate at arbitrary γ in Eq. (37) in Ref. [8]. The asymptotic behavior for $\gamma \ll 1$ reduces the rate to tunnel effect of the exponential form. At $\gamma \gg 1$, the ionization rate takes the multi-photon power law form.

Under our experimental conditions, the evaluation of Eq. (2.15) leads to $\gamma \sim 2$ for the laser at the threshold intensity $I_{th} = 1.2 \times 10^{13}$ W cm^{-2}. At this region the two assimptotic forms for $\gamma \gg 1$ and $\gamma \ll 1$ are both ill-defined and the evaluation of the complete form of $W(I)$ is needed.

Figure 2.4 shows the nonlinear transmission as a function of the input laser pulse energy. The solid blue line presents the experimental results for 800 nm 45 fs laser absorption in fused silica. The absorption threshold is around 50 nJ. The dot-dashed green curve shows the modeling results, where ionization rates were defined by Keldysh formalism. There is a good agreement between the experiment and the theory around the breakdown threshold and at the absorption level up to 15%. For stronger absorption and higher electron density the plasma defocusing starts affecting the laser propagation and the experiment starts deviating from theoretical predictions.

However, numerical modeling using full Keldysh formalism is time consuming. We compare the ionization rates obtained with Eq. (37) from Ref. [8] and the power law $W(I) = \sigma_6 I^6$ at the intensity level corresponding to

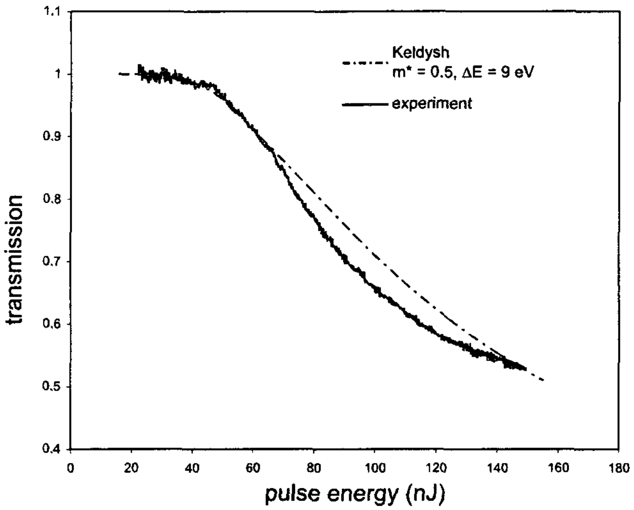

Figure 2.4: Transmission as a function of the input pulse energy. Solid blue – experimental results for 800 nm 45 fs laser pulses focused (NA = 0.25) through a fused silica slab (Suprasil I). Dot-dashed green – self-limiting propagation model (Eq. (2.6)) using $W(I)$ from Eq. (37) from Ref. [8] and avalanche coefficient $\beta = \alpha_0 I$, $\alpha_0 = 4$ J^{-1} cm^2 as in [25].

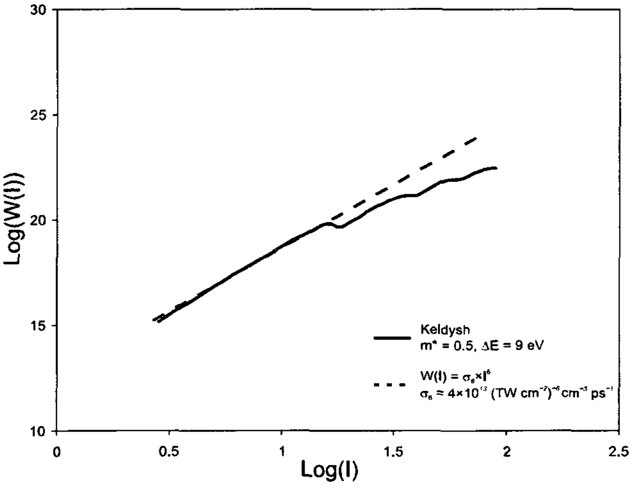

Figure 2.5: Ionization probability as a function of the laser intensity. Solid red – $W(I)$ from Eq. (37) from Ref. [8]. The electron effective mass, m* = 0.5 m$_e$, $\Delta = 9$ eV. Dashed blue – $W(I) = \sigma_6 I^6$, where $\sigma_6 = 4 \times 10^{13}$ (TW cm^{-2})$^{-6}$ cm^{-3} ps^{-1}.

$I_{th} = 1.2 \times 10^{13}$ W cm^{-2}. For this intensity regime, there is a good agreement between the two methods with multi-photon ionization cross-section, $\sigma_6 = 4 \times 10^{13}$ (TW cm^{-2})$^{-6}$ cm^{-3} ps^{-1}. For example, we use this value of σ_6 to study nonlinear memory effect in fused silica [19].

In Fig. 2.5 we show the ionization rates for 800 nm laser in SiO_2, obtained using Keldysh formalism (red solid) and $W(I) = \sigma_6 I^6$ (blue dashed) for different laser intensities. In the range of $I = 10^{13}$ W cm^{-2}, the two curves overlap.

We can use the simplified power law for multi-photon absorption modeling when material properties, such as electron mass or band gap are uniform. However, in order to describe the strong field ionization in crystals, we apply the full Keldysh formalism to study the effect of the electron reduced mass tensor on the ionization probability [12].

The Keldysh model also allows to extend the analysis of nonlinear absorption into the region of attosecond science. Here the sub-laser-cycle variation in the ionization yield can be derived from polarization sensitive absorption measurements [13].

2.5 Avalanche and "Cold" avalanche

We have so far treated avalanche ionization, $\beta(I) = \alpha_0 I$, as a linear process with respect to the laser pulse intensity. However, in nonresonant multiphoton ionization of atoms, re-collision electrons can stimulate non-sequential double ionization — the single atom analogue to avalanche ionization [24]. It is now recognized that ionization can also occur for a low energy collision where the intense laser field assists the collision [18]. In other words the re-collision creates a double excited state that has a significantly lowered tunneling barrier and consequently ionizes readily. In solid-state device physics, photon assisted tunneling is well known. Here it is absorption of a photon rather than a collision that contributes the energy, but the effect in both cases is lowering of the tunneling barrier. Photon assisted tunneling is also applied in scanning tunneling microscopy [36]. We show that collision assisted tunneling (or field assisted collisional ionization) also plays a role when intense laser pulses interact with dielectric materials.

In the electron rate equation (2.5) avalanche ionization is described by $\beta(I)$. We first consider the simplest case where $\beta(I) = \alpha_0 I$. We use the flux doubling model [32] to evaluate $\alpha_0 I$. In this model, the probability of impact ionization reaches 100% when the kinetic energy of the conducting electron reaches the threshold value, $U_{th} \sim \Delta$. The parameter α_0 defines the heating rate to energy U_{th} and is given by Eq. (2.16).

$$\alpha_0 = \frac{2p}{\varepsilon_0 c \int_0^{U_{th}} {}^1\!/_{\sigma(\epsilon)} d\epsilon}, \tag{2.16}$$

where p takes a value between 0.5 and 1 and $\sigma(\epsilon)$ is the conductivity per electron at electron energy, ϵ, given under the Drude formalism by Eq. (2.17).

$$\sigma = \frac{e^2}{m^*} \frac{\tau_c(\epsilon)}{(1 + \tau_c^2(\epsilon)\omega^2)}. \tag{2.17}$$

Here e is the electron charge, ω is the laser frequency, m^* is the reduced mass of the electron and $1/\tau_c(\epsilon)$ is the electron energy, ϵ, dependent electron-phonon momentum collision rate. For $\tau_c(\epsilon)$ independent of ϵ, and with $p = 1$, α becomes simply $\alpha = 2\sigma/\varepsilon_0 c U_{th}$.

We propose that, in the flux doubling context, field assisted or "cold" avalanche lowers the effective collisional ionization threshold. The concept is shown schematically in Fig. 2.6. In this picture, traditional avalanche is described by the pumping rate $\alpha_0 I$ to the threshold U_{th} where collisional

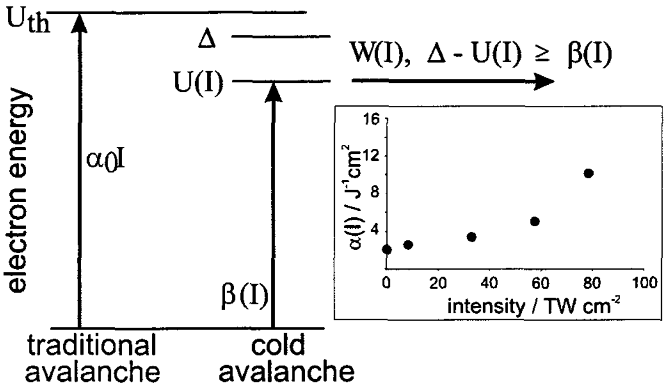

Figure 2.6: Schematic rate description of traditional and cold avalanche ionization. U_{th} is the collisional ionization threshold. In the absence of an external field the avalanche rate, $\alpha_0 I$, is determined by the heating rate to this level. In the presence of an external field the effective threshold, $U(I)$ is determined as the energy at which the multi-photon ionization rate, $W(I)$, for the reduced band gap, $\Delta - U(I))$, exceeds the heating rate to that energy level, i.e the ionization probability approaches 1. Δ is the band gap. Insert: Dependence of the avalanche coefficient, $\alpha(I)$, on intensity estimated using the flux-doubling model.

ionization is effectively instantaneous. In the presence of a strong laser pulse this threshold is lowered due to field assistance. The extent depends on the field.

The threshold in the presence of the field, $U(I)$, is the electron energy at which the heating rate is exceeded by the collision assisted ionization rate, $W(I)$, for the reduced band gap, $\Delta - U(I))$. $W(I)$ increases as the effective band gap decreases. We can determine the intensity dependence of the avalanche coefficient by replacing U_{th} with $U(I)$ in Eq. (2.16). If we assume τ_c is independent of ϵ, with $p = 1$ the result for $\beta(I) = \alpha(I)I$ is $\alpha(I) = 2\sigma/\varepsilon_0 c U(I)$, or, in terms of α_0 (Eq. (2.18))

$$\alpha(I) = \frac{\alpha_0 U_{th}}{U(I)}. \tag{2.18}$$

The insert in Figure 2.6 shows the result for $\alpha(I)$ obtained by comparing multi-photon rates based on the Keldysh formalism with $\alpha(I)$ from Eq. (2.18).

The reduction in the threshold energy U_{th} implies a different heating rate α. One way to describe the dependence of the avalanche ionization on the laser field, $\beta(I)$, is by a perturbative approach, similar to all nonlinear optics phenomena, that is field or intensity dependent. Here we substitute $\beta(I)n$ term in rate equation (2.5) with a laser intensity power series to include the cold avalanche:

$$\frac{dn}{dt} = W(I) + n \times \alpha_0 I(1 + \sum_{j=1}^{k-1} \beta_j I^j). \tag{2.19}$$

In the brackets we include the multi-photon contribution to collisional ionization with "colder" electrons, $\beta_j I^j$. The colder the electrons, the higher the multi-photon order j.

Experimentally we can directly obtain the $\beta(I)$ and therefore α_0 and β_j values from numerically fitting transmission measurements done with different pulse durations. These experimental results are shown in Fig. 2.7(top). From the figure we find that the threshold energy required for the onset of the multi-photon absorption increases with the pulse duration. This result is expected, since ionization is not energy, but intensity dependent process. The careful analysis of the curves in Fig. 2.7 shows that the threshold energy increase does not depend linearly on the pulse duration. The bottom panel in Fig. 2.7 shows the threshold energy as the function of the pulse width.

We fit the experimental transmission curves by numerical analysis of the pulse propagation through the focus, taking non-linear absorption and carrier generation into account through Eq. (2.6), where $\beta(I) = \alpha I$ [7, 9]. We model $W(I)$ as $\sigma_k I^k$ where k is the multi-photon order and σ_k is the kth order cross-section. We use $k = 6$ and $\sigma_6 = 4 \times 10^{13}$ (TW cm^{-2})$^{-6}$ cm^{-3} ps^{-1} as in Ref. [19]. Note that, for judging the quality of the fit, we concentrate on the region close to the threshold. At transmission levels below 75% the formation of sufficiently dense plasma in the focal volume modifies the laser beam refraction and invalidates the assumption of Gaussian beam propagation. In all our analysis we concentrate on absorption around I_{th} where focusing remains unchanged by the interaction.

Using the above parameters for $W(I)$ and $\alpha = 4$ J^{-1}cm^2, the top panel in Fig. 2.8 compares fits (long dashed red) made to transmission curves (solid black) collected using 43 and 1260 fs pulses. The agreement with experiment is only good for $\tau = 43$ fs. For 1260 fs, the model underestimates the experimental threshold by a factor of almost two. Also shown is the fit (short dashed blue) to the 1260 fs data, using the same value of σ_6, but smaller $\alpha = 2.2$ J^{-1} cm^2. This fits the data well. A sensitivity analysis shows that σ_6 has to be changed by an unrealistic amount to have the same effect as the factor of ~ 2 change in α.

For different pulse durations (between 43 fs and 1260 fs, shown in top

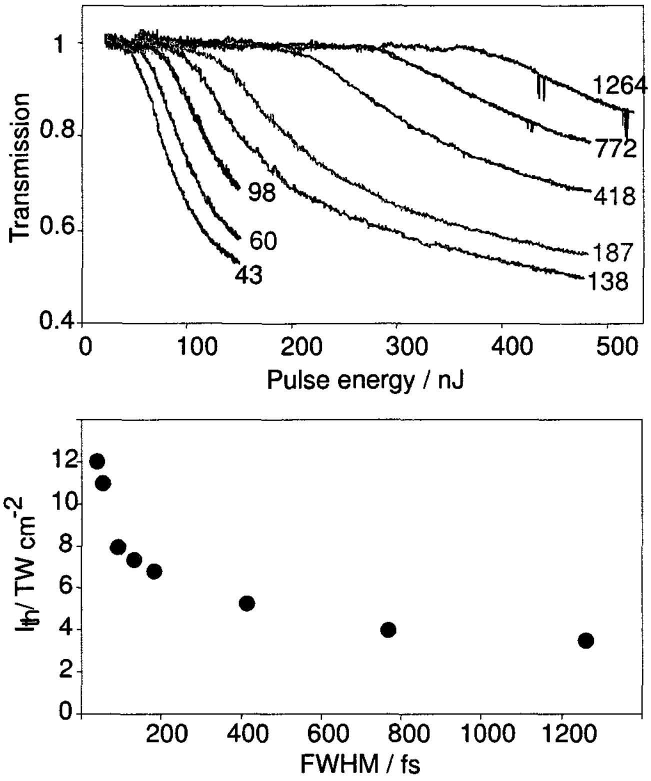

Figure 2.7: (top) Pulse width dependence of the transmission of femtosecond laser pulses through a tight focus in fused silica as a function of the incident pulse energy. The curves are labeled by their FWHM in femtoseconds. (bottom) Threshold intensities, I_{th}, obtained from the transmission curves, as a function of pulse width.

part of Fig. 2.7 we adjust α to fit the model to the experiment. The results for α are shown in Fig. 2.8. The effective avalanche rate is higher for shorter pulses where laser intensity is higher. We repeat the fitting procedure, keeping fixed σ_6 value and adjusting $\beta(I)$ for all curves shown in Fig. 2.7. Figure 2.8(bottom) shows the dependence of α on pulse length. The results demonstrate, unexpectedly [30], that the avalanche rate is higher for shorter pulses.

During field assisted collisional ionization, the multi-photon contribution to avalanche ionization should have a number of terms as shown in Eq. (2.19). The maximum intensity reached inside the material is clamped at the level of I_{th} by non-linear absorption. In the case of fused silica $I_{th} \leq 1.2 \times 10^{13}$ W cm^{-2} (Fig. 2.7 bottom). At this intensity the photon flux is ~ 1 photon

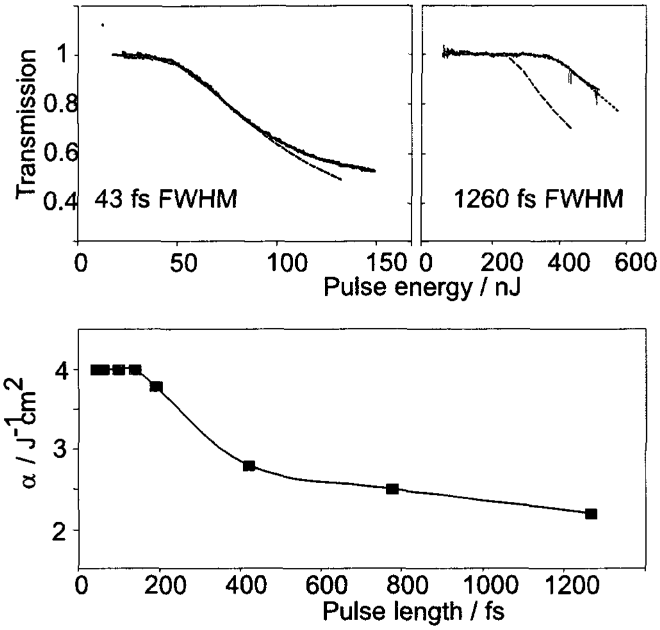

Figure 2.8: (top) Numerical fits to the transmission vs pulse energy curves for pulses of 43 and 1260 fs FWHM including traditional avalanche through Eq. (2.5). The solid, noisy curves are the experimental results. The red, long-dashed line in both panels is obtained with $\alpha = 4$ J^{-1}cm^2. The blue, short-dashed line in the left panel is obtained with $\alpha = 2.2$ J^{-1}cm^2. In both cases the multi-photon rate, $W(I)$, is taken as $\sigma_6 I^6$ with $\sigma_6 = 4 \times 10^{13}$(TW cm^{-2})$^{-6}$ cm^{-3} ps^{-1}. The transmission curves cannot be modeled globally using a single value of α. (bottom) The avalanche coefficient, α, derived as a function of pulse length by fitting the transmission curves, keeping σ_6 fixed.

per Å^{-2} per 300 attosecond, i.e one photon in the expected lifetime of the electron-atom collision complex. Higher orders of j are much less likely in this intensity range making the $j = 1$ term in Eq. 2.19 dominant under our conditions.

Figure 2.9 shows the result of a global fit to all the transmission curves using single values of α_0 and β_1, independent of τ. The fits were obtained with $\alpha_0 = 1.7$ J^{-1}cm^2 and $\beta_1 = 1.7 \times 10^{-13}$ W^{-1}. Again we approximate $W(I) = \sigma_k I^k$ with $k = 6$ and $\sigma_6 = 4 \times 10^{13}$ (TW cm^{-2})$^{-6}$ cm^{-3} ps^{-1}. Considering the global nature of the fit the agreement is good.

By including a single, low-order term to describe cold avalanche we successfully model nonlinear absorption in fused silica for pulses from 43 to 1260 fs. Due to intensity clamping our results apply to cold avalanche at low inten-

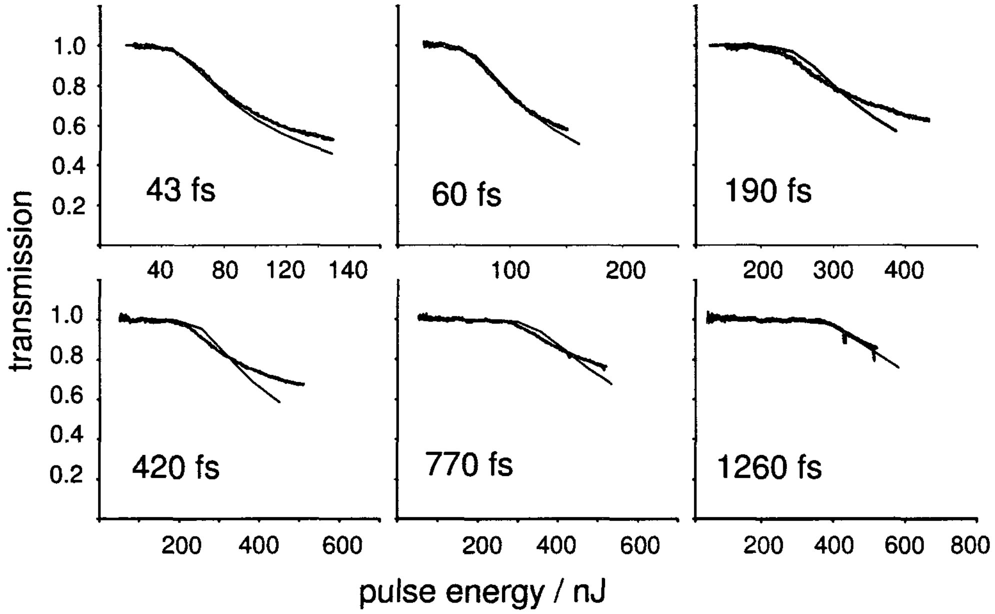

Figure 2.9: Transmission vs pulse energy curves for pulses in the range 43 to 1260 fs FWHM. The solid, noisy curves are the experimental results. The red, long-dashed lines are fits obtained globally by including cold avalanche through the carrier generation rate given by Eq. 2.19, with $\alpha_0 = 1.7$ J^{-1}cm^2, $\beta_1 = 1.7 \times 10^{-13}$ W^{-1} and $j = 1$. The multi-photon rate, $W(I)$, is taken as $\sigma_6 I^6$ with $\sigma_6 = 4 \times 10^{13}$ (TW cm^{-2})$^{-6}$ cm^{-3} ps^{-1}.

sities. From the low order of j we also understand that in cold avalanche, as it operates inside solids under intensities moderated by non-linear absorption, most of the ionization energy is still contributed by the collisions. However, a significant increase in the avalanche rate can come from absorption of a single photon. Indeed photon assistance can contribute even for relatively long pulses and can help explain the success of flux-doubling models that assume the band-gap as the collisional ionization threshold [32] in describing what has been thought of as traditional avalanche ionization. Realistically the threshold for pure collisional ionization is significantly above the band gap, however the presence of even a modest field will bring this threshold down to the band gap. Our results suggest that cold avalanche ionization persists at least up into the picosecond pulse regime.

In conclusion, we have demonstrated a method of studying light interaction with dielectrics that has sufficient precision to confirm field assisted avalanche. This extends the concept of field assisted collisional ionization all the way from single atoms to solids. In bulk dielectrics the light intensity never becomes very large so field assisted tunneling increases the avalanche coefficient by only a factor of ~ 2. However, at the surface of dielectrics the situation is different. High intensities can be reached because the pulse is not attenuated before the focus by non-linear absorption. The order of assistance to the collision will be much higher in this case. Comprehensive models for laser machining and laser damage in dielectrics need to take cold avalanche into account.

In this chapter we have presented the way to analyze material breakdown with intense laser pulses, by the analysis of the transmitted laser light. We have shown the analytical model that predicts the pulse energies for the onset of nonlinear absorption for short (up to 100 fs) laser pulses. We have presented an extended theory that deals with collisional ionization at different regimes of the laser intensity, that predicts the breakdown behavior at surfaces at high laser intensities.

Our models helped explain the experimental observations of nonlinear memory [19] and nano-structures formation [37]. They have extended to study lattice effects in the ionization of crystals [28], provide attosecond resolution in ionization dynamics [12] and enhanced transmission effect [38].

In the next chapter we will build on this approach to obtain even more detailed information on the breakdown process. We will show the extension of our measurements into the regime of sub-laser cycle resolution.

Chapter 3

Attosecond Metrology inside Solids

In this chapter we show the way to the ionization measurements with attosecond resolution inside solids. We use the inherent pump-probe nature of the elliptically polarized femtosecond laser light to demonstrate the sub-laser cycle dynamics of the multi-photon breakdown inside transparent dielectrics. We access the attosecond time scale by measuring the differential absorption between the major and the minor axes of the polarization ellipsoid. The cross-over from breakdown dominated by multi-photon absorption to avalanche ionization is clearly observed. The method can be generalized to two color pump-probe absorption experiments for higher time resolution.

Multi-photon ionization of atoms and molecules by intense infrared laser light and re-collision assisted ionization [24] are characterized by sub-laser period dynamics. The range of phases over which the electron appears in the continuum increases as the order of the nonlinearity decreases [39]. In the tunneling limit, the electron appears near the field maximum because tunneling is exponentially sensitive to the field strength. In contrast, the phase sensitivity is completely lost for single photon transitions. The sub-cycle nature of multi-photon ionization is a basis of all current attosecond optical technology [40]. One should expect similar dynamics in wide band gap dielectrics where band-to-band transitions are analogous to ionization and where avalanche ionization shares features with re-collision assisted ionization. In gases, re-collision generated attosecond XUV pulses [40] can be used to probe attosecond dynamics of ionization [41]. However, a solid, except at its surface, is not accessible to XUV light due to strong absorption and dispersion.

However, as we have seen, wide band gap, ΔE ~10 eV, dielectrics are transparent for low intensity 800 nm femtosecond light. When the intensity enters the multi-photon ionization regime, the density of photons is still much less than the density of the solid. The beam is significantly depleted when only about 0.1 percent of the atoms are ionized. As long as the plasma density is kept low, depletion is directly related to the ionization probability [7]. By measuring the characteristics of the transmitted fundamental beam, we obtain information on multi-photon ionization in solids. Until now, in solids, only the pulse envelope has been analyzed, ignoring any sub-cycle information it carries. Experiments in gases with elliptically polarized laser light showed how high harmonic emission carries the ionization information with attosecond resolution [42]. We will show that in solids, where high harmonics cannot be observed, harmonic generation alters the polarization of the fundamental field. While the information is less complete than when attosecond pulses are used [41], probing the ellipticity changes provides the sub-cycle dynamical resolution to the ionization process in the bulk.

3.1 Polarization effects in Multi-photon Absorption

We measure the intensity dependent change of elliptically polarized light in fused SiO_2. Using 43 fs 800 nm radiation we find that first as we increase the pulse intensity the major axis of the ellipse rotates as the intensity increases, while the ellipticity remains constant. This is dominated by 3rd order nonlinear effects and ellipse rotation is well known [35]. Then, once we enter the highly nonlinear absorption regime, ellipse rotation ceases. Instead, the ellipticity increases with intensity. In other words, in the highly nonlinear regime, transmission depends on the phase. Absorption maximizes near the peak of the field – the major axis of the ellipse – and is minimum when the field points toward the minor axis.

Sub-cycle effects should disappear once inverse Bremsstrahlung and avalanche ionization dominate the absorption, since neither collision process is phased with the laser field. This is precisely what we measure. The change in ellipticity is less if we use 160 fs pulses and by the time we reach 180 fs pulses it falls below our noise floor. Thus, the ellipticity changes of a pulse allow us to separate contributions from multi-photon ionization and from avalanche ionization.

Our approach to measuring sub-laser-cycle dynamics is motivated by the early work of F. Brunel [43]. Brunel studied low-order harmonic generation due to tunnel ionization in atoms. He showed that a step - like increase in the electron density in the continuum leads to the generation of odd harmonics that are out of phase with the ionizing laser field. In other words, the total field is re-shaped to limit its peak value. While not considered by Brunel, the fundamental field must also be affected. Therefore, for the first experiments and to avoid the deleterious dispersion effects in SiO_2, we use only the 800 nm light.

The experiment was performed with 800 nm, 43 fs (FWHM) pulses which could be stretched by tuning the grating compressor to a longer pulse. We used a microscope objective with numerical aperture of 0.25 to focus the laser beam $\sim 150\mu$m inside fused silica sample. Our pulse energies ranged from 20 nJ to 300 nJ corresponding to intensities between 0.5×10^{13} and 7×10^{13} W cm^{-2} if the focus were in vacuum. The transmitted beam was collimated using an identical microscope objective. By translating the sample, we ensured fresh material for each laser shot.

We controlled the polarization of the input beam with a quarter wave plate before the focusing objective. We analyzed the transmitted polarization using a rotating polarizing prism. The transmitted light was then measured on a photo diode. For elliptical polarization, the signal on the photo diode follows a function $y = \cos^2(\phi) + \epsilon^2 \sin^2(\phi)$, where ϕ, is the polarizer rotation angle relative to the major axis of the polarization ellipsoid of the incident light, and ϵ, is the ellipticity. It can be measured as $\epsilon = \sqrt{\min(y)/\max(y)}$.

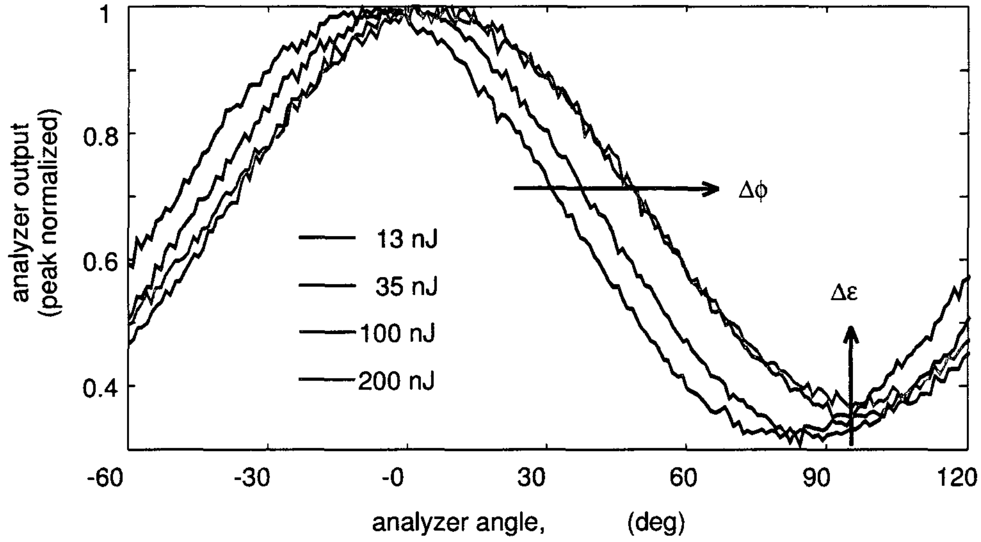

Figure 3.1: Polarization state analysis of the transmitted light. Peak normalized transmission through polarization analyzer as a function of its angle. Input pulse energies are shown in the legend. The horizontal shift is due to the ellipse rotation (→). The change of the minimal value is due to the ellipticity increase (↑).

Figure 3.1 shows the polarization state of the transmitted laser light for four different incident pulse energies. The curves are normalized for convenience. The figure shows that, as laser pulse energy increases, the ellipsoid rotates and ϵ increases. The position of the curve with respect to the analyzer angle, ϕ, shows the orientation of the polarization axis. We can see that the curves corresponding to 35 nJ and 100 nJ are progressively shifted with respect to the lowest 13 nJ case (as shown with the horizontal red arrow). This effect is the ellipse rotation.

The rotation of the ellipse is a $\chi^{(3)}$ effect [35]. The direction of the ellipse rotation follows the polarization handedness of the incident light and the amount of rotation, $\Delta\phi$, grows linearly with laser intensity. In Fig. 3.2(a) a solid line connecting data points shows that $\Delta\phi$, measured in Fig. 3.1, saturates after the onset of absorption (the vertical line located at the inflection point of the dotted transmission curve).

The second energy dependent effect in Fig. 3.1 is the increase in the minimal value of the curves (the vertical green arrow). With the peak of the curves normalized to 1, the minimal value is a direct measurement of the square of the field ellipticity. This minimal value ($\epsilon \approx 0.58$) remains constant for 13 nJ and 35 nJ and increases for 100 nJ and even more so for 200 nJ. The ellipticity starts changing toward a more circular at the pulse energies above the multi-photon absorption threshold.

Figure 3.2(b) shows the changes in the ellipticity, $\Delta\epsilon$, as a function of the input pulse energy for a 43 fs pulse and compares it with the transmission curve. For pulse energies below the breakdown threshold the ellipticity remains constant, $\Delta\epsilon = 0$. With the start of the absorption, the ellipticity starts increasing and it reaches the maximum change of 10% (ϵ(250 nJ)$\approx$0.64).

When longer pulse durations are used, the contribution of collisions in absorption increases through strong inverse Bremsstrahlung and avalanche ionization. In these cases we expect less re-shaping of the laser electric field and, therefore, minimal changes in the ellipticity of the transmitted light. For the 115 fs pulse (Fig. 3.2(c)) the ellipticity change is smaller than for 43 fs and it reaches only $\Delta\epsilon = 5\%$. In the case of 180 fs pulse (not shown) the ellipticity change is below our experimental noise level.

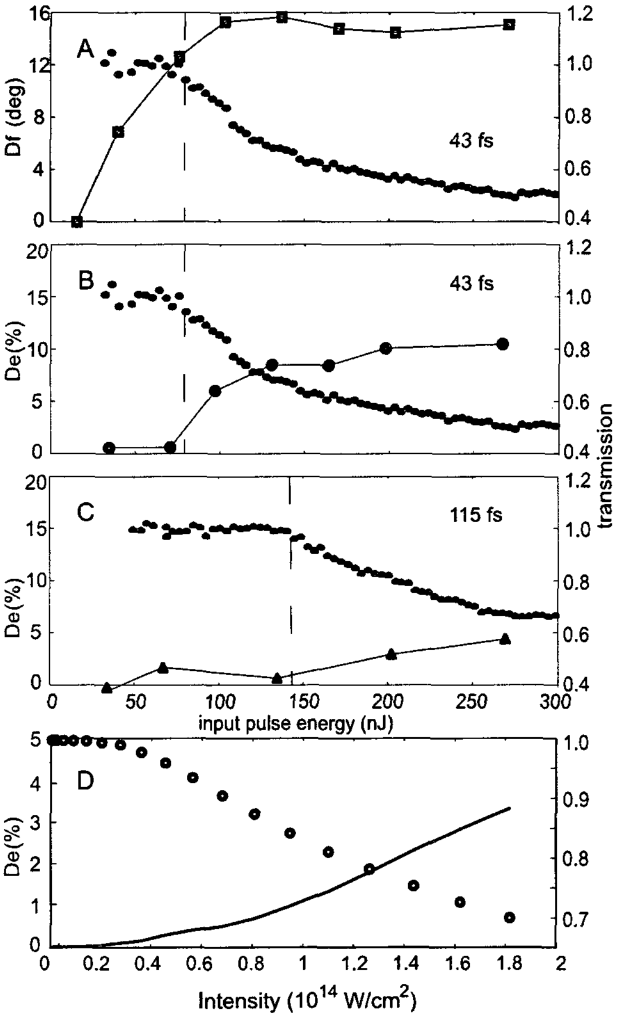

Figure 3.2: (a,b,c) Experimental results. Transmission (green o) and (a) – ellipse rotation, $\Delta\phi$, (blue □), (b,c) – ellipticity change, $\Delta\epsilon$, (red o (b) and △ (c)) as a function of the incident pulse energy. Pulse duration 43 fs (a,b) and 115 fs (c). Input ellipticity $\epsilon = 0.58$ in all cases. (d) Numerical modeling results. Transmission (blue circles) and ellipticity (solid red) as a function of the input intensity.

3.2 High Density Gas Model

To support our interpretation, and to allow us to explore a wider range of parameters than would be feasible in a single experiment (such as the use of a fundamental pulse together with its low harmonics) we employ a dense atomic gas model, solving numerically the Maxwell propagation equation

$$\left[\frac{\partial^2}{\partial z^2} - \frac{1}{c^2}\frac{\partial^2}{\partial t^2}\right]\vec{E}(z,t) = \frac{4\pi}{c^2}\frac{\partial^2}{\partial t^2}\vec{P}(z,t)$$

and the Schrödinger equation for a one-electron atom

$$i\frac{\partial}{\partial t}\Psi(\vec{r}_\perp,t;z) = \left[-\frac{1}{2}\frac{\partial^2}{\partial \vec{r}_\perp^2} + V(r_\perp) - \vec{r}_\perp \cdot \vec{E}(z,t)\right]\Psi(\vec{r}_\perp,t;z)$$

where $\vec{r}_\perp$ is coupled through the atomic polarization $\vec{P}(z,t) = N\langle\Psi(\vec{r}_\perp,t;z)|\vec{r}_\perp|\Psi(\vec{r}_\perp,t;z)\rangle$, N is the atomic density. All equations are in atomic units.

For linearly polarized light the problem reduces to a one-dimensional case, where, $r_\perp = x$ is the electronic coordinate and z is the laser propagation direction. The atomic binding potential, $V(r_\perp) = -0.6\exp[-4\ln 2(r_\perp/1.7)^4]$, chosen to give a single bound state with ionization potential $IP = 9$ eV equal to the SiO_2 band gap. Before the pulse arrives, all of the atomic population is in the ground state. Absorbing boundary conditions (complex or 'optical' potentials) are used to model the loss of coherence of the electron due to electron-lattice scattering. The boundaries smoothly attenuate the wave function over the range of 17 to 30 au [44].

Figure 3.3 illustrates how the envelope of an ionizing pulse is affected by absorption. For the calculation we used an input light intensity of $I_0 = 1.5 \times 10^{14}$ W cm^{-2}, an 800 nm pulse with duration (FWHM) of 20 fs, and a density of $N = 5 \times 10^{-4}$ au. This density corresponds to an average atomic separation of 6 Å, thus our model is less dense than typical solids but still dense enough to support macroscopic absorption. In the calculation we filter the field to only pass frequencies up to the 4.5 times the fundamental frequency. We do this because, in solids, the dispersion and the absorption of laser higher harmonics is very strong.

Figure 3.3 shows the changes in the pulse intensity envelope that occur due to absorption at different propagation depths, L. The input pulse at L = 0 μm has a Gaussian intensity envelope. Following the strongest absorption between L = 0 and 4 μm, the pulse intensity is clamped below the level where there is significant ionization. There is almost no difference between the 8 and the 12 μm curves. This basic behavior is captured in an approximate model Ref. [7] that allows an analytical description of laser absorption in solids.

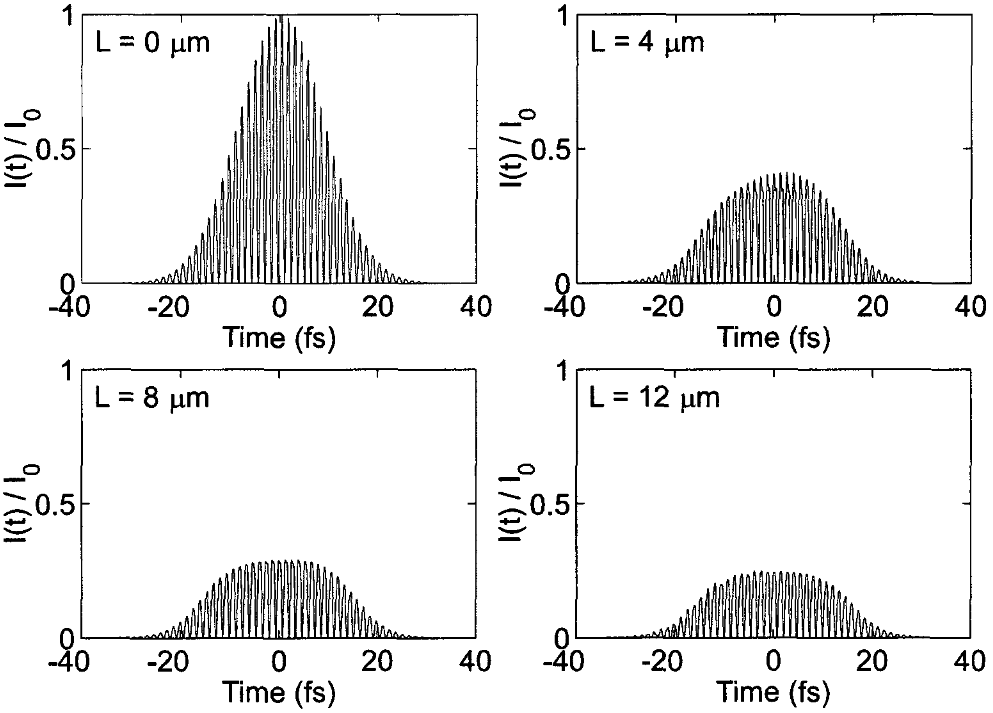

Figure 3.3: Numerical modeling results for laser intensity temporal profile as a function of the propagation depth.

Next we extend the dense atomic gas model to 2D to describe the propagation and the absorption for elliptically polarized light. Now $\vec{r}_\perp = (x, y)$, $r_\perp = \sqrt{x^2 + y^2}$ and the binding potential $V(r_\perp) = -0.945 \exp[-4 \ln 2 (r_\perp/2)^4]$, again chosen such that $I_p = 9$ eV. In Fig. 3.2(d) we compare the changes in ellipticity, as a function of the pulse energy, with transmission. The figure shows that the ellipticity remains constant for the low input pulse intensities, below the ionization threshold. At higher intensities the $\Delta\epsilon$ (solid line) increases, indicating the change in polarization toward a more circular. The behavior qualitatively agrees with experimental results shown in Fig. 3.2(a-c). The change $\Delta\epsilon = 3.5\%$ for 70% transmission is in good agreement with our experiments considering the simplicity of the model.

Elliptical polarization experiments provide only limited time resolution. The model allows us to explore how combinations of harmonic radiation can

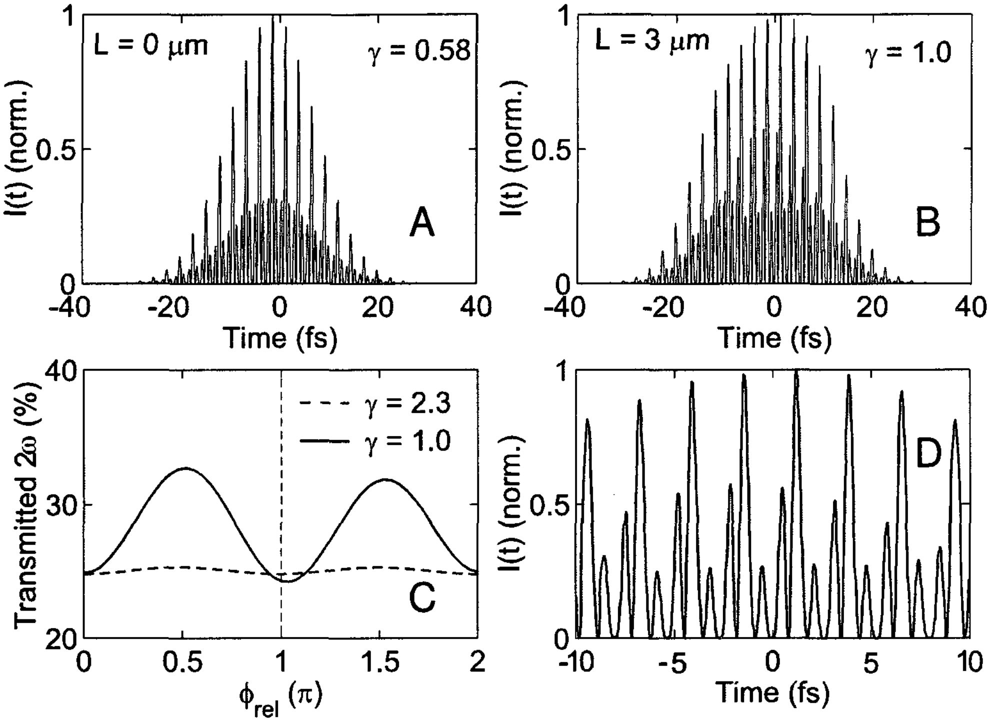

Figure 3.4: Intensity of $\omega + 2\omega$ field before (a) and after (b) absorption. (d) Pulse reshaping, zoom–in on (b). (c) Phase-dependent absorption of a 2ω probe for two intensities of accompanying fundamental pulse.

be used to yield higher time resolution. We illustrate the opportunity by studying the fundamental and its second harmonic. In centro-symmetric media, where even harmonics are not produced, the two colors, ω + 2ω, provide the most intuitive way to probe the sub-cycle absorption. Figure 3.4 demonstrates these ideas.

Figure 3.4 shows the pulse profile at the input to (a) and after (b) propagating through absorbing high density gas. The initial pulse, at L = 0 μm, is combined of two frequency fields, ω and 2ω, of equal intensity. Qualitatively the peak–normalized pulse profile consists of strong peaks with ω periodicity and side-bands at the level of 0.25. With propagation depth, the pulse intensity drops (as in Fig. 3.3) and the field reshapes. The reshaping of the field (see the zoom–in in Fig. 3.4(d)) occurs due to the phase sensitive absorption in multi-photon ionization. The absorption starts at the highest points of the field and extends for $\sim \pi/2$ radians that follow. This results in the asymmetric shape of the pulse. At L = 3 μm, the left side-band, less absorbed, is at the level ~0.5 and the right side-band is absorbed together with the peak and appears at ~0.25 level.

Sub-cycle absorption is largely expected when the Keldysh parameter, γ, [8] is of the order or smaller than 1. Due to pulse absorption and the resulting intensity drop, γ increases with L, as indicated on the figure. Strong differential absorption within a cycle is observed between $L = 0$ and $3\ \mu$m, where $\gamma < 1$. For $L > 3\ \mu$m, $\gamma > 1$ the absorption is uniform through the laser cycle and the ratio between the side-bands and the main peaks remains unchanged (not shown).

Sub-cycle absorption can be probed with higher precision by scanning a phase delay, ϕ_{rel}, between the strong fundamental pulse and its weak SH. Figure 3.4(c) shows how the transmission of the second harmonic signal is modulated with ϕ_{rel}. The two curves show results for two pump intensities corresponding to different values of γ. The total absorption in both cases was 25%. For $\gamma = 2.3$, absorption is almost uniform through the laser cycle and the modulation in the SH transmission is negligible. For $\gamma = 1$ the probe transmission is strongly modulated due to sub-cycle absorption. Maximum absorption occurs ~3.5 deg after $\phi_{rel} = 0$ and π, right after the peaks of the 2ω pulse line up with the peaks of the fundamental and the total field magnitude is the highest. The delay for the otherwise symmetric time-dependent electric field may indicate the breakdown of the quasi–static regime of ionization.

3.3 Tunneling rates with Elliptical polarization

In atoms and molecules an analytical expression has been derived [39] to describe the instantaneous ionization rates for different laser intensities, I_l, and ionization potentials, IP, and, therefore, arbitrary Keldysh parameter γ [8]. Here the ionization rate includes both phase independent, or multi-photon, rate and phase dependent rate, or tunneling. This calculation predicts (with exponential accuracy) that for linear polarization, $\gamma \sim 2$ and IP = 9 eV, the ratio between the ionization rate at the zero of the laser field (multi-photon "background") and the peak is ~ 0.18.

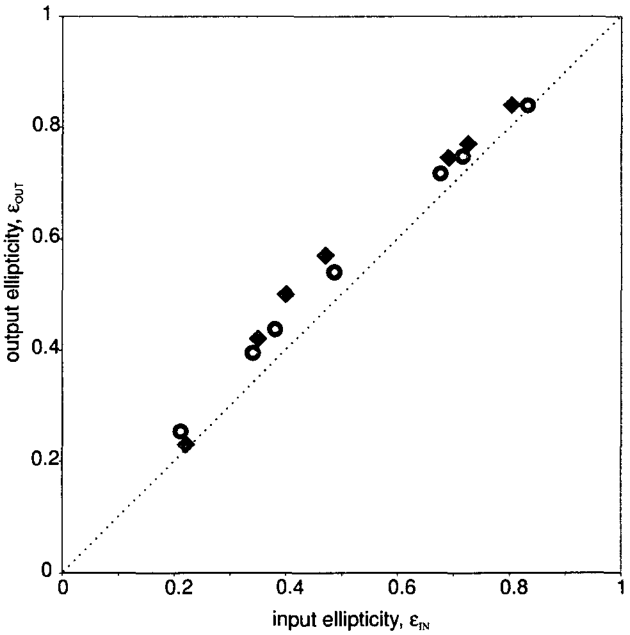

Figure 3.5: Ellipticity of the transmitted laser light as a function of the input ellipticity. Pulse energy 80 nJ in all cases. o - fused silica absorption experiment, ■ - theory [39].

From this model [39] we learn that, for a constant input pulse energy, the multi-photon rate decreases when polarization changes from linear, $\epsilon = 0$ to circular, $\epsilon = \pm 1$. This results in stronger instantaneous rate variation across the cycle with bigger $|\epsilon|$. For $\epsilon = 0.6$, the ratio in the rates between the zero and the peak of the field, drops to 0.02.

From the variation in the sub-laser cycle ionization yield predicted in [39] we can calculate the change in the laser polarization, assuming linear relationship between ionization yield and absorption. Figure 3.5 shows the experimental and the theoretical results for the changes in ellipticity for fixed input pulse energy. The ellipticity of the transmitted laser light after absorption is plotted against the ellipticity of the incident beam. The pulse energy in all cases remained 80 nJ.

The deviation in both the experimental and the theoretical points from the 45° line indicate that the transmitted polarization is changed toward more circular due to tunneling ionization. The magnitude of the ellipticity change depends both on the value of the input ellipticity and the peak intensity of the field. From Fig. 3.5 it is clear that the optimum input ellipticity for the sub-cycle dynamic measurements is around 0.6 as we have used in the experiments.

To conclude this chapter, we have demonstrated an approach to attosecond metrology in transparent materials. It is based on a single laser beam polarization measurements where strong ellipticity changes are used to probe the sub-cycle nature of multi-photon absorption. By changing the laser wavelength we will be able to observe the transition from tunneling to perturbative multi-photon ionization. Extending the method to crystalline solids where, as we will show, the tunneling probability depends on the alignment between the laser electric field and the lattice [28] we can probe the influence of carrier mass on tunneling dynamics, since carrier mass changes affect γ.

For few cycle laser pulses polarization changes due to absorption can lead to a new metrology for the carrier envelope phase. Since only nJ pulse energies of the fundamental laser pulse are needed, attosecond measurements offer the potential for the in vivo phase control.

At longer wavelength the fundamental and its second harmonic can be chosen to have the same dispersion in the sample. Without the phase walk-off in the interaction region, these experiments are poised to provide a higher temporal resolution for the attosecond metrology in the bulk. It is important to apply the technique to pre-ionized (e.g. doped) materials, where avalanche ionization dominates the interaction or for very short pulses, where new avalanche mechanisms are predicted [11, 29].

Chapter 4

Multi-Photon Crystallography

In chapters 2 and 3 we have shown how femtosecond laser breakdown inside solids can be studied using nonlinear transmission. We now extend the method to crystalline materials. In this chapter we show how using multi-photon ionization one can probe crystal structure of solids. Using different crystalline dielectrics we show that the multi-photon ionization probability depends on the lattice symmetry. Information on the symmetry is transferred to the laser field via the dependence of the nonlinear absorption on the sample orientation. The multi-photon nature of the interaction allows us to probe the crystal symmetry locally, anywhere in 3-dimentional sample. We show that the structure of crystal quartz is not changed by repeated illumination of the focal region with 45 fs pulse.

For intense laser pulses, multi-photon ionization rates in molecules depend on the shape of the highest occupied molecular orbital and on its alignment with respect to the electric field [14, 18]. Experiments in the gas phase with aligned N_2 and O_2 showed differences of more than 50% in the ionization yield depending on the angle between the linearly polarized laser electric field and the molecular axis [15, 16]. As we have seen, transparent dielectrics have band gaps comparable to the ionization potential of such molecules and therefore should exhibit similar behaviour. This would give us a structural probe of crystalline dielectrics that can follow local phase change with femtosecond precision and micrometer spatial resolution.

4.1 Crystal Symmetry Probe

We realize multi-photon crystallography by measuring the dependence of the transmitted light on the alignment of the crystal with respect to the laser polarization direction. We show that the alignment dependence of the multi-photon ionization probability depends on crystal symmetry. Since multi-photon ionization confines the interaction to a small region of the laser focus [45] this implies that we have a highly local probe of crystalline structure, anywhere in 3-dimensional space. By using an optically contacted interface between fused and crystalline quartz, we confirm the local nature of the interaction.

Our calculations [7] show that the temperature rise induced by the probe is proportional to the pulse duration and is approximately 110 K for a 45 fs pulses at 10% absorption. The temperature increase would be only 12 K if a 5 fs pulse were used. Thus probing crystal structure via multi-photon crystallography should not affect the crystal especially, if a few-cycle pulse is used. Using 45 fs pulses we show that the crystal structure of α-quartz is not changed by multiple laser shots at the same spot.

We have studied α-quartz (α-SiO_2), sapphire (α-Al_2O_3) and lithium fluoride (LiF) and amorphous fused silica as a control. The first two are birefringent and were z-cut to reduce associated complications. The LiF was cut square to its cubic lattice. We used linearly polarized 45 fs, 800 nm laser pulses with a repetition rate of 40 Hz to 400 Hz. A microscope objective with numerical aperture of 0.25 focused the laser beam. The focus was $\sim 150\mu$m inside the sample unless otherwise noted. This tight focusing allows us to reach high intensities without propagation being influenced by low order effects such as self-focusing or self-phase modulation. In our experiment the pulse energies used were in the range of 20 nJ to 300 nJ to give intensities between 0.5×10^{13} W cm^{-2} to 7×10^{13} W cm^{-2} if the focus were in vacuum.

The crystals were placed on a translation stage to provide new material every laser shot if required. The crystals were mounted with their z-axes parallel to the laser k-vector. A half wave plate was placed in the incident laser beam to control its polarization alignment relative to the lattice. All transmitted light was collected by an integrating sphere and the signal was acquired independently for every laser shot.

Figure 4.1 shows the nonlinear transmission as a function of alignment angle for α-quartz with zero degrees corresponding to alignment of the laser electric field vector and the crystal x-axis. By eye one can discern two dominant modulation periods, of $\sim 60°$ and $\sim 180°$, in the transmission. We apply a Fourier analysis technique to examine the modulation in more detail.

We measure the alignment dependence of the transmission while rotating

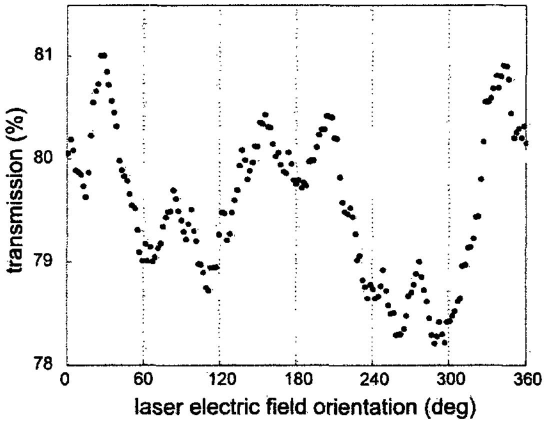

Figure 4.1: Transmission measured in α-quartz as a function of the alignment of the laser polarization to the crystal x-axis. A 10 points moving average has been applied to the raw data.

the half wave plate at $6\frac{2}{3}$rpm. Signal modulation frequencies are obtained by discrete Fourier transform. The results for the three crystals are shown in Fig. 4.2. The ordinate in the figure is the modulation amplitude as a percentage of the average transmission, which was set to 0.8 by choice of the laser pulse energy. The abscissa is the recurrence frequency of the alignment angle, where 2 corresponds to rotation period of π (or two-fold rotational symmetry), 4 - $\pi/2$, 6 - $\pi/3$. Fused (amorphous) silica (not shown) has no modulation. All crystal samples show strong Fourier features. α-Quartz and sapphire both show modulation with π and $\pi/3$ rotational periods. The latter corresponds to their trigonal lattice system. The π modulation is due to a residual birefringence and is discussed below. LiF has a cubic unit cell and shows strong $\pi/2$ periodicity. It is clear that the absorption of intense femtosecond pulses measures the symmetry of the lattice (Fig. 4.2 (bottom)).

We now confirm that the angle dependent changes in the linear or low-order non-linear [35] refractive index do not contribute to our measurements. By doing so we also confirm the high spatial resolution in the z direction. We use an optically bonded sample of fused and crystal SiO_2. With this sample we repeat the Fourier transmission experiments for different positions of the focus relative to the fused silica – α-quartz interface. Experimentally we identify the surface by the small reflection (0.4%). The surface position is established (zero in Fig. 4.3) by forcing the reflection to retrace the optical path.

The results for the two peaks in Fig. 4.2, corresponding to the 2- and 6-fold symmetries, are presented in Fig. 4.3. The two peaks have differ-

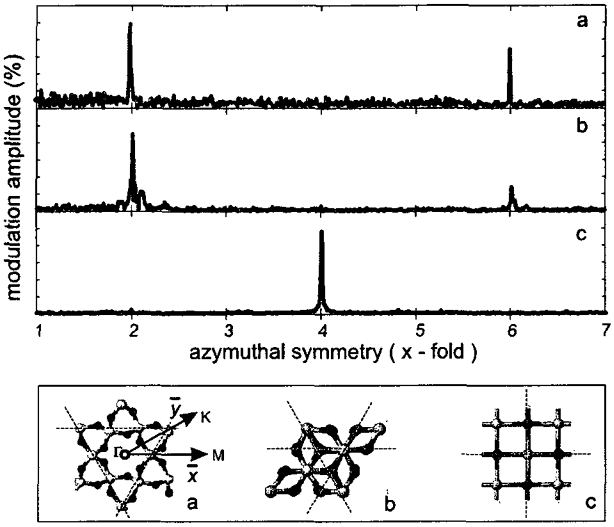

Figure 4.2: Non-linear transmission modulation spectra for (a) α-quartz, (b) sapphire and (c) lithium fluoride. The vertical scale is 0 – 0.75% for (a,b) abd 0 – 1.5% for (c). Corresponding crystal structures (the bottom panel) [46, 47] (z-cut view) are shown looking down the z-axis with dashed lines as eye-guides for the symmetry.

ent dependence on the focus position. The magnitudes of both peaks are zero before the interface when the absorption occurs in fused silica and is azimuthally symmetric. When the focus approaches the interface, the crystalline structure shapes the absorption and the 6-fold peak rises sharply. The 6-fold peak maximizes when the focus meets the interface. There is almost no signal change after the focus is fully inside the crystal. Therefore, linear or low-order nonlinearities do not contribute significantly to the angle dependent absorption.

A 2-fold peak also appears only inside the α-quartz, but its magnitude grows more slowly with focus depth. This is typical for linear and Kerr - like propagation effects that increase with interaction length. However, in our experiment, the 2-fold peak is due to a combination of the birefringence experienced by peripheral laser beams (due to strong focusing) and residual, angle-dependent ellipticity that is due to imperfect alignment of the rotating half wave plate. This parasitic birefringence induces an angle and depth dependent ellipticity at the focus that modulates multi-photon ionization via the effective intensity. Notably the 2-fold peak is absent from amorphous fused silica and non-birefringent LiF, but is also present in birefringent sapphire.

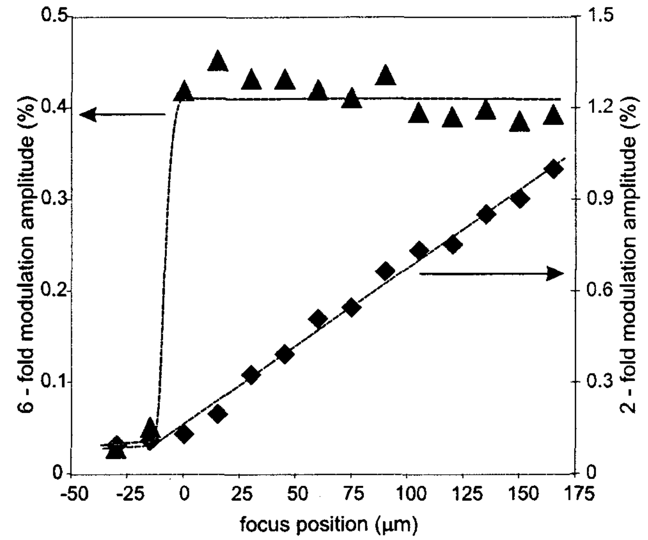

Figure 4.3: The amplitude of the 6-fold (▲) and 2-fold (◆) modulation in transmission as a function of focus position, z, in an optically bonded fused silica and α-quartz sample. The focus is in fused silica for negative z and in α-quartz for positive z. The pulse energy was 90 nJ.

All of the results presented so far were obtained using a fresh spot for every laser shot. We use a model developed in Ref. [7] which is based on the calculations of the electron density in the conduction band due to field ionization and avalanche. Using the modeled carrier density, we can estimate the associated temperature rise, assuming that all energy absorbed from the laser pulse for the purposes of ionization and electron heating is transferred to heat [7]. For α-quartz a 20% absorption of 45 fs pulse causes 156 K heating with every laser shot. The heat dissipates completely between shots. To confirm that the crystal is not modified by the measurement, we apply the method to measure any changes in crystal structure that may accumulate from laser shot to laser shot. We measure crystal structure at a given point as function of the number of shots. Over our measurement range (1 to 1000 shots) we see no change.

The dependence of the absorption on the alignment of the crystal lattice to the laser field implies that the multi-photon ionization rate, $W(I)$, is dependent on the alignment angle, ϕ. An analytical approach to high-order non-linear absorption in dielectrics is to approximate the interaction by an intensity threshold, I_{TH}, below which light is not absorbed and above which all of the light is absorbed ($W(I) = 0$, $I < I_{TH}$; $W(I) = \infty$, $I > I_{TH}$). This leads to the "lawnmower" description of non-linear adsorption in dielectrics

[7]. Under this model a modulation of $W(I)$ with ϕ translates to a modulation in I_{TH}. A feature of the model is that the transmission, T, depends on the input intensity, I_{IN}, in a manner that includes I_{IN} only as the ratio I_{IN}/I_{TH} or, in terms of pulse energy, E_{IN}/E_{TH}. The consequence is that we can write $\partial T/\partial E_{TH} = -E_{IN}/E_{TH} \cdot \partial T/\partial E_{IN}$, implying that $\Delta T \propto -E_{IN}\partial T/\partial E_{IN}$, where ΔT is the modulation in the transmission.

Since any highly nonlinear absorption will behave in much the same way, in Fig. 4.4 we compare the measured amplitude of the 6-fold modulation with the quantity $-E_{IN}\partial T/\partial E_{IN}$ as a function of E_{IN}. We obtain $\partial T/\partial E_{IN}$ by numerical differentiation of the measured T vs E_{IN} dependence at a fixed angle (the choice of angle is not crucial as the modulation in T is small). It is clear that the 6-fold modulation shows the energy dependence expected, confirming that this modulation relates to an angle dependence of the rate of multi-photon ionization.

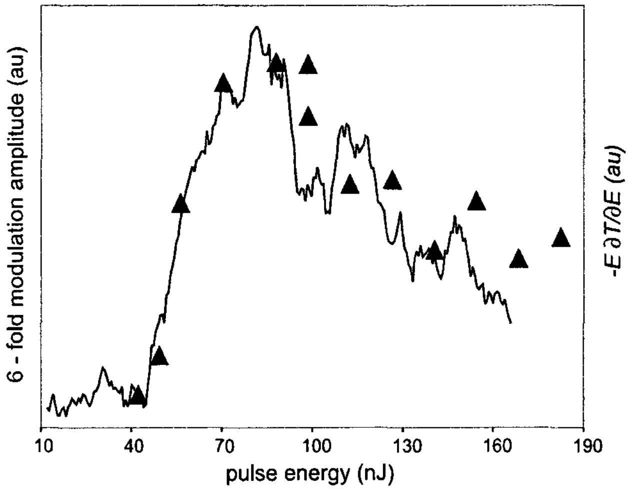

Figure 4.4: Comparison of the energy dependence of the 6-fold transmission modulation in α-quartz with the expectation from an alignment dependence of multi-photon ionization. (▲) 6-fold transmission amplitude; (—) the quantity $-E_{IN}\partial T/\partial E_{IN}$ with $\partial T/\partial E_{IN}$ obtained as the numerical derivative of the transmission measured as a function of E_{IN}. The two series of data have been normalized for comparison purposes.

4.2 Reduced Mass Effects

In small gas phase molecules, alignment effects relate to the symmetry of the ionizing molecular orbital. In crystals the electronic structure is discussed in terms of band structure not orbitals. Theory on tunneling in solids that traces back to Zener [48, 49] predicts that

$$W(I) \propto \exp\left(-\frac{(2\Delta)^{3/2}\sqrt{m^*}}{3e\hbar\mathcal{E}}\right) \tag{4.1}$$

where $\mathcal{E}$ is the electric field. The expression is very similar to the equivalent one for an atom except that the band gap, Δ, replaces the ionization potential, the electron mass becomes the reduced mass, m^*, and the exponent is reduced by a factor of 2. Thus we expect multi-photon tunnel ionization in solids to depend exponentially on the band gap, just as it depends on the ionization potential in atoms and molecules. In addition, in crystals, $W(I)$ also depends exponentially on the reduced mass of the electron, a quantity that is also related to the band structure.

The explicit treatment of the effective mass in crystals as a tensor quantity in the theory of tunneling ionization, was first introduced by Keldish in Ref.[50]. However, in his later widely used work [8], the spatial asymmetries of the effective mass were ignored.

Concentrating on α-quartz, we have obtained the band structure from theory, using the pseudopotential plane-wave method with the ABINIT code [51, 52, 53]. Trouiller-Martins-type [54], generalized gradient approximation pseudopotentials were employed with a Perdew-Burke-Ernzerhof exchange-correlation functional [55]. Inspection of the band structure shows that the minimum vertical band gap occurs at the Γ symmetry point. It is, therefore, direction independent and cannot be the cause of the transmission modulation.

The reduced mass, however, is dependent on the direction in the crystal. In reciprocal space the α-quartz structure is characterized by two symmetry points, M and K. The associated directions, Γ-M and Γ-K, in real space are depicted in Fig. 4.2. They lie at an angle of $\pi/3$ to each other and line up with the crystal x and y axes respectively. Because the curvatures of the highest valence band and the lowest conduction band depend on direction, the reduced mass of the electron responding to an aligned field is effectively different.

The reduced mass of the electron is a concept that is only easily defined for a parabolic band structure. This is not the detailed case in α-quartz, but we obtain representative values of the reduced mass along different directions in the crystal from the calculated electronic energy levels using parabolic fitting. The estimated reduced mass changes from 0.93 m_e along Γ-M, to 2.15 m_e along the Γ-K direction. Therefore, from Eq. 4.1, we expect the ionization to be the most probable along the Γ-M direction where the reduced mass is the smallest. In our transmission experiments we found that absorption is at its maximum when the laser polarization is parallel to Γ-M or x-axis, and at its minimum when the laser field is along Γ-K (at 30° to Γ-M), in agreement with the theory. Due to the exponential dependency of the tunnelling rate on the band gap value, we only consider transitions between the top valence band and the bottom conduction band.

From Eq. 4.1 the differences estimated in m^* imply a much larger transmission modulation than is found in the experiment. Translated into a threshold model they imply a threshold increase of about ×2. One possible cause is the two band approximation in our final tunneling calculation. The lower degree of modulation found experimentally may be partially due to ionization not being in the tunnelling limit. At a laser wavelength of 800 nm with an intensity of 3×10^{13} W cm^{-2} the Keldysh parameter, γ, is ~ 1. In this regime tunnelling still plays a role in atoms [39], but its contribution is limited. The role of tunnelling decreases at shorter wavelengths with the increase in γ. We have repeated the crystallographic experiments with 400 nm laser radiation for α-quartz and LiF crystals. In the perturbative regime ($\gamma > 1$) we do not expect an exponential dependence on m^* [8]. We found that in α-quartz the modulation in transmission was not observed at 400 nm where the band gap is only three photons wide. In LiF, where four photons are required for ionization, the modulation is present. These results are consistent with the Keldysh analysis and suggest that the modulation is connected with tunnelling.

It is interesting to compare the origins of angle dependent tunnelling in molecules and crystals. In molecules, interference between components of the tunnelling electron wave packet, arising from different components of the parent orbital, is responsible for the angle dependence of the ionization probability [14, 18]. In crystals, similar mechanisms may be in play but the ionization dependence is dominated by the direction dependent reduced electron mass since it appears in the exponent (Eq. 4.1).

To conclude this chapter, tunnelling plays a major role in solid state physics. Usually tunnelling is driven by DC fields. We have shown that optical fields can be effectively used, broadening the range of potential applications. This opens a route to measure the dynamics of femtosecond phase changes far away from any surface.

Looking to the future, multi-photon crystallography can be applied in the mid-infrared extending access to important semi-conductor materials such as gallium nitride and silicon. It will be possible to map out crystal size, orientation and position in polycrystalline material. The technique is non-destructive, especially if few-cycle pulses are used. Although we have concentrated on non-birefringent z-cut material, this was only a convenience not a necessity.

Multi-photon crystallography adds to the array of multi-photon microscopies available to science, providing a superior spatial resolution due to the higher nonlinear nature of the process. Its use of only one laser wavelength removes phase walk-off constrains for the in-the-bulk measurements, compared to the multi-colour methods.

Chapter 5

Material Reorganization

In this chapter we move from measurements to control. We show the different ways transparent dielectrics reorganize following multi-photon ionization. The material modification provides a positive feedback mechanism, the basis for material modification. Using nonlinear transmission and beam refraction, we study the molecular-scale changes in the material that lead to the reduction in the multi-photon ionization rates, the "nonlinear memory", and the macroscopic restructuring, leading to the formation of the defocusing micro-lens, "enhanced transmission" and "second harmonic memory".

So far our aim has been to measure basic ionization process occurring in transparent materials. We have neglected the chemistry. In chapters 2, 3 and 4 we have analyzed the many aspects of strong field and collisional ionization in pristine materials. Experimentally we achieved this by operating at relatively low repetition rates of the laser and translating the sample between laser shots. This ensured fresh material at every shot.

In this chapter we irradiate the same spot in the material with multiple laser pulses. If the intensity of the laser field is not too high, ionization triggers chemical changes in the material. When multiple laser shots fall on the same volume in the sample, the material changes induced by ionization accumulate. These changes can provide a feedback mechanism to the ionization process.

- In section 5.1 we demonstrate a shot-to-shot reduction in the threshold laser intensity for ionization of bulk glasses illuminated by intense femtosecond pulses. For SiO_2 the threshold change serves as positive feedback re-enforcing the process that produced it. This constitutes a memory in nonlinear ionization of the material. The threshold change saturates with number of pulses incident at a given spot. Irrespective of the pulse energy, the magnitude of the saturated threshold change is constant ($\sim 20\%$). However the number of shots required to reach saturation does depend on the pulse energy. Recognition of a memory in ionization is vital to understand multi-shot optical or electrical breakdown phenomena in dielectrics. The material restructuring leads to small changes on the refractive index, $\Delta n \sim 10^{-3}$, inside the focal volume, used in waveguide writing.

- In section 5.2 we will show that with repeated illumination, even minute changes in the molecular structure, observed only through nonlinear interaction with laser field, result in the localization of the ionization centres and the formation of nano-structures. These macroscopic changes in the material in the focal volume such as the formation of nano-voids, modifies locally the refraction properties of the material, leading to the laser intensity changes inside the sample, and as a result, the material breakdown. In technology nano-cracks are used for writing micro-fluidic channels with and without chemical etching. Ordered nano-voids can be used in building polarization selective micro-optical devices.

By repeatedly illuminating fused silica slabs with focused femtosecond pulses, we permanently decrease the local refractive index without increasing linear absorption or scattering. This progressively forms a bi-convex lens in the pre-focal region. With linearly polarized light, the index change reaches several percent and is associated with the formation of an array of planar nano-cracks. We analyze the polarization-dependent focusing power of the sub-wavelength periodic structure. While the detailed material modification changes, spontaneous defocusing lens formation is a common feature of every wide band gap transparent materials that we have studied (SiO_2, BK7, LiF, sapphire, mica).

- In section 5.3 we will describe the "enhanced transmission effect". We will show that the gradual formation of the defocusing micro-lens is associated with the reduction of the multi-photon absorption. The breakdown threshold energy in fused SiO_2 increases 3 times compared with the fresh material, when the micro-lens is formed.
- In the last section 5.4, we will show a specific type of material modification, observed in crystal. By repeatedly ionizing quartz sample with femtosecond pulses, we create permanent material modification with favorable phase-matching for the second harmonic generation. The conversion efficiency for second harmonic generation is $\sim 1\%$ and is limited by the laser intensity inside the bulk. The buildup of the second harmonic memory depends on the alignment between the crystal and the laser field. This effect is accompanied with the formation of the defocusing microlens in the interaction region.

5.1 Nonlinear Memory

Intense, non-resonant femtosecond light pulses will ionize bulk atomic [10] or molecular gases [56], transparent liquids [57] or solids [58], when focused inside them, through nonlinear interaction with the material. However, solids are unique in that the material in the focal volume remains in place between laser shots. Any nonlinear laser induced chemical changes will accumulate and the laser-modified material constitutes a feedback mechanism — or a nonlinear memory in the system. Current models of intense light interaction with dielectrics [58, 9, 59] do not take this memory effect into account, yet it can be very important. If chemical changes lower the ionization threshold, then the feedback on the ionization process is positive and any plasma non-uniformities will be reinforced. Such a mechanism has been proposed [37] to play a pivotal role in the formation of ordered nano-structures in fused silica following femtosecond laser irradiation [34, 60]. Feedback must influence the interaction and evolution of any nonlinear phenomena developing over multiple shots.

We demonstrate the existence of such a feedback by measuring the transmission of the ionizing pulse through the material. We find that the ionization threshold reduces if the material has been previously ionized. The change, which appears to be permanent, is not caused by scattering or resonant absorption since transmission in the low intensity linear regime remains unchanged. We measure that the ionization threshold for fused silica is 1.2×10^{13} W/cm^2 on the first shot and that the threshold reduces on each laser shot until it reaches a saturation value that is 20% lower. We show that the saturated threshold is independent of the peak pulse energy. However, we find that the rate at which the threshold approaches the saturated value depends on the free carrier density in the focal region and therefore on the pulse energy.

In a multiphoton context, a 20% reduction in the threshold is large. Because of the nonlinear interation it corresponds to a large local difference in absorption. Thus our results show a new kind of nonlinearity where chemical change provides feedback that can drive a shot-to-shot nonlinear interaction. No laser-induced breakdown process in dielectrics will be free of this nonlinearity.

Our work is related to experiments that have observed incubation effects on damage thresholds for light interacting with dielectric surfaces and bulk glass [25, 61, 62, 63]. The causes of these incubation effects are not well established due to the complexity of the damage process. As ionization is the first step in this process it is likely that nonlinear memory is important here too.

For our experiment we used 40 fs, 800 nm pulses from a Ti:Sapphire laser operating at 400 Hz. The pulses are focused inside the glass samples mounted on precision XY stages, using a 0.25 NA microscope objective. A combination of a half-wave plate and a polarizer controls the intensity of incident light. The input beam is pre-chirped to compensate for material dispersion.

We use integrating spheres to monitor both the incoming light fluctuations and the transmitted light (see Fig. 2.1). This ensures that the transmitted beam is collected completely, even if scattered or defocused by the plasma formed by ionization. The transmission is measured on a shot-to-shot basis using a computer-controlled data acquisition system.

Figure 5.1 illustrates some of the main characteristics of the nonlinear memory in SiO_2. With the laser firing at 400 Hz the transmission was measured on a shot by shot basis while the pulse energy was ramped up to 100 nJ and then back down again without moving the focal spot.

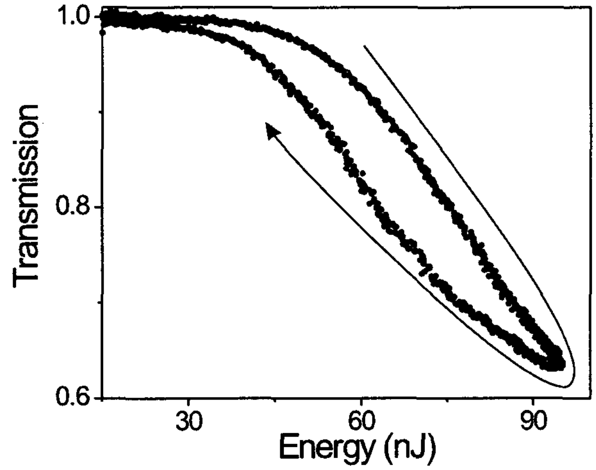

Figure 5.1: Nonlinear absorption hysteresis inside fused silica. Transmission is plotted as a function of pulse energy. Keeping the laser focus at a fixed spot the energy is ramped up from shot to shot and then back down. The full cycle consists of 17000 shots. The arrow shows the path of increasing number of shots.

The figure emphasizes four major features of the interaction. (a) The transmission drops monotonically from unity with the initiation of ionization - it defines an ionization threshold. Beyond this threshold, the transmission is reduced with increase in pulse energy. (b) The transmission curve does not retrace when energy is decreased, indicating a memory induced in the material by the previous laser shots. Since the focus is fixed, the total number of shots incident at the spot increases continuously during the experiment. (c) The ionization threshold is indeed reduced with a previous history of ionization. (d) There is no change in transmission at low energies - the memory can be observed only if the pulse energy exceeds the ionization threshold. Thus, the memory is inherent to nonlinear ionization and not caused by the cumulative damage in the material.

Figure 5.2 zeroes in on the nonlinear memory that is uncovered by the hysteresis-like behavior when the laser intensity is increased and then decreased. It shows the transmission of an ionizing pulse as a function of number of laser shots in SiO_2. The pulse energy is 160 nJ, approximately three times the ionization threshold of fresh material. Following the first shot, the solid circles in the figure show that the transmission of every subsequent shot monotonically decreases and saturates after a few thousand shots. Even at these energies, there is no damage induced at the focal spot that affects transmission. This is verified by measuring the transmission of low energy pulses (10 times below the ionization threshold) through the irradiated spot and a fresh spot. Within the accuracy of our measurements there is no difference in transmission (Fig. 5.2 inset). Thus the memory exists in nonlinear ionization itself.

The open circles in Fig. 5.2 show the transmission at the same spot after a delay of 1 hour. There is no loss in nonlinear memory after one hour. It is impractical to maintain alignment through the same spot for extended periods but we have qualitative evidence that the memory is permanently embedded in the material. This is further supported by the fact that the magnitude of the transmission change remains invariant of the laser repetition rate from 40 Hz to 100 kHz.

Having shown the existence of the nonlinear memory and how it evolves as a function of the number of shots, we now quantify the change by modelling the transmission. Our approach is based on the self-limiting absorption model for bulk dielectrics that recognizes that nonlinear absorption depletes the beam as it propagates towards the focus [7, 9]. It is a unique feature of multiphoton ionization in condensed media that an ultrashort laser pulse will be depleted of photons long before the medium is depleted of un-ionized atoms. For example, the density per unit area of atoms over the focus is given by $n_a z$ where n_a is the atomic density and z is the confocal parameter of the laser beam. The comparable fluence is $I\tau/kh\nu$ where I is the light intensity, τ the pulse duration, $h\nu$ the photon energy and k the number of photons absorbed. If $z = 10\mu\text{m}$, $n_a = 2 \times 10^{22}\ \text{cm}^{-3}$, $\tau = 50$ fs, $h\nu = 2.5 \times 10^{-19}$ J and $I = 10^{13}\ \text{W/cm}^2$, all typical numbers, then there are 100 times more atoms available than can be ionized by the pulse.

Figure 5.3 compares the transmission curves of fresh glass (obtained by

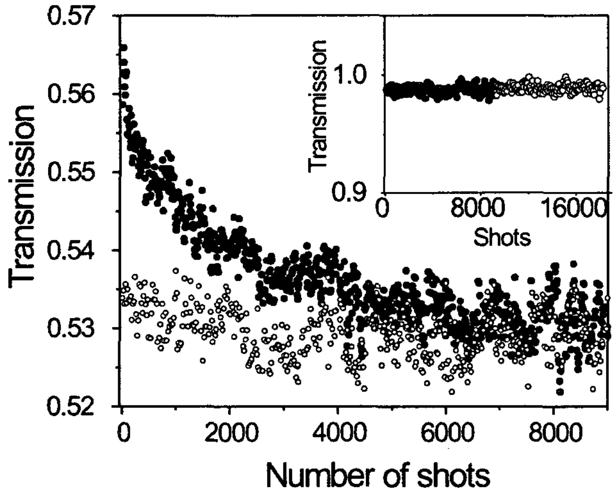

Figure 5.2: Nonlinear absorption as a function of exposure at a fixed pulse energy (160 nJ). Transmission is plotted as a function of the number of laser shots. The solid circles are the result of starting in material that has not been exposed previously. The open circles show the transmission through the same spot having left the laser off for 1 hour. The inset shows the transmission at low intensities before (open circles) and after (solid circles) the irradiation, demonstrating that the memory only operates in the nonlinear regime.

moving the sample between shots) and glass that has previously been exposed to 10000 shots at 160 nJ/pulse, sufficient to saturate the memory effect. The solid line fits are obtained by solving the self-limiting model numerically and include avalanche ionization, with the carrier generation rate given by

$$\frac{dn}{dt} = \alpha I n + W(I) \tag{5.1}$$

where α is the avalanche coefficient and $W(I)$ is the nonlinear ionization rate. Here we have chosen to approximate the absorption rate as $W(I) = \sigma_k I^k$ where k is the multiphoton order and σ_k is the k^{th} order cross section. The fits take into account the fact that the profile of the laser beam at the focus of our 0.25 NA objective was found to be approximated by a super-Gaussian rather than a Gaussian. Both fits were obtained with α set at 4 $J^{-1}cm^2$ the same as the value obtained by Lenzner *et al.* from measurements of damage thresholds on fused silica surfaces [25].

Given the 9 eV band gap of fused silica the appropriate value of k is 6.

For the fresh glass we found $\sigma_6 = 4 \times 10^{13}$ (TW cm^{-2})$^{-6}$cm^{-3}ps^{-1} and for the memory saturated glass we found $\sigma_6 = 1.6 \times 10^{14}$ (TW cm^{-2})$^{-6}$cm^{-3}ps^{-1}, an increase of a factor of 4. These cross sections are of the same order as those predicted by Keldysh theory for a band gap of $\sim$ 9 eV for ionization in the multi-quantum absorption regime [8]. The drop in ionization cross section indicates a permanent change in the material that effectively reduces its band gap. The departure of the fit from the transmission results at high pulse energy is attributed to plasma defocussing that is not taken into account in the model.

Ionization thresholds are another useful approach to quantify changes in the nonlinear interaction. We obtain such thresholds, I_{th}, by alternatively fitting the transmission curve using a model that approximates $W(I)$ to a step function, i.e. $W(I) = 0$ for $I < I_{th}$ and $W(I) = \infty$ for $I > I_{th}$. For a Gaussian beam profile the transmission as a function of pulse energy can be described analytically [7] but to allow for the super-Gaussian beam profile used in our experiments we carry out the modelling numerically. Because this simple model does not include avalanche ionization and we are primarily interested in obtaining the ionization threshold, we fit only the early part of the transmission curve. The results are shown as the dashed lines in the figures. We find an ionization threshold of 1.2×10^{13} W cm^{-2} for fresh fused silica and a threshold of 9.5×10^{12} W cm^{-2} for material where the memory effect has been saturated.

Similar results are obtained with laser pulse energies up to at least 550 nJ, about ten times the threshold. The only difference is that the rate at which the memory is established changes. The memory effect always saturates at a drop in threshold of $\sim$ 20%. The memory effect is also observed with laser pulse widths of up to at least 2 ps.

From Fig. 5.2 and related plots made at other pulse energies we obtain first-order rate coefficients for the rate of change in transmission with number of laser shots. The results are plotted in Fig. 5.4. The rate constant first increases with pulse energy but then reaches a maximum value and remains constant. This is a signature of the self-controlled nature of energy deposition inside dielectrics by nonlinear absorption.

The solid line on the same curve is the calculated peak plasma density in the focus of the laser pulse, calculated numerically when applying the self-limiting model as described above. The curve shown was obtained with the plasma generation rate given by Eq. 5.1 and using the same values of α and σ_k used to produce the fits to the transmission results plotted in Fig. 5.3. The plasma density saturates as a consequence of the pulse being depleted by nonlinear absorption before it reaches the focus. Clearly the data points fall almost on the plasma density curve given that one point is used

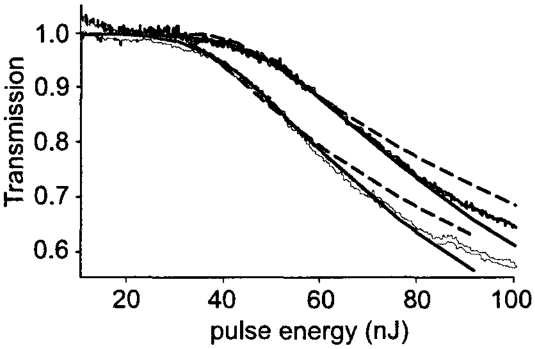

Figure 5.3: Modelling nonlinear absorption to characterize the memory. Transmission is plotted as a function of laser pulse energy. The experimental curve showing the higher threshold (blue in the on-line version) is obtained by moving the sample so that fresh material is irradiated on each shot. This curve forms a baseline for assessing the memory effect. The lower threshold curve (red on-line) is obtained at a single spot after exposure to 10000 shots at 160 nJ. This is sufficient to saturate the memory effect. The solid lines through the data are fits from numerical modeling that includes nonlinear absorption due to multiphoton and avalanche ionization and considers pulse propagation as described in the text. The dashed lines show fits of a simple sudden onset analytical model, that neglects avalanche, to the early portions of the transmission curves. This fit can be used to obtain threshold intensities as also described in the text.

to determine a scaling factor. The rate constant describing the change in threshold is proportional to the number of electron-holes that are generated.

The nonlinear memory appears to have a common origin with femtosecond dielectric modification in SiO_2 and other dielectrics. In fact a lowering of the threshold for nonlinear absorption signals a lowering of the band-gap in SiO_2 which would indeed increase the refractive index as is observed [6]. Raman experiments indicate that there is a chemical change in which the five and six membered rings that dominate the local order in amorphous SiO_2 shrink to predominantly from three to four membered rings [64, 65]. The modified nonlinear threshold could arise from this modification, or from the many defects that are almost certainly generated by this process. Like the memory effect, both the refractive index changes and the changes in Raman response are known to show saturation with exposure [66, 65].

To conclude this section, we have measured a feedback mechanism in the nonlinear ionization of SiO_2 with ultrashort pulses. It manifests itself as a lowering of the ionization threshold. We have shown that the rate of

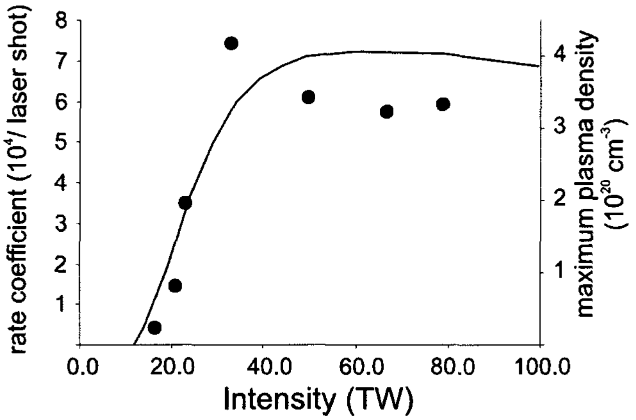

Figure 5.4: The rate coefficient for the change of transmission with number of laser shots (referred to the left axis) as a function of the peak pulse intensity that would be obtained in the absence of absorption(•). The line (referred to the right axis) plots the calculated maximum plasma density reached per shot as obtained by numerical modeling as described in the text.

reduction depends on the plasma density that is reached in the material. If this is correct at microscopic levels, then inhomogeneities in the break down will grow as a result of this positive feedback. We expect that such inhomogeneities can build into nanoplasmas whose interaction with strong fields can play a large role in the formation of ordered nano-structures during dielectric breakdown [37].

Nonlinear memory is likely to be a general feature of dielectric breakdown when it occurs inside the dielectric. We observe it in BK7 glass, where colour centres play a partial role and in SiO_2 where chemical changes appear to dominate. It may occur in crystalline media where the crystalline structure is modified, or in polymers where more complex chemistry can occur. However, in all of these cases, if the laser pulse is very short the pulse contains insufficient energy for conventional damage. Unusual nonlinear phenomena are likely to occur.

Next we increase the number of pulses from 10^3 to 10^6 and find an even stronger response. We create nano-voids that can modify the refractive index much more. In the next chapter we will show that strong changes in the refractive index affect the laser refraction.

5.2 Formation of Defocusing Micro-lens

Microfabrication is primarily based on lithographic technologies. These are especially advanced in microelectronics for the fabrication of ultra high-density devices. The approach contributes also to the large field of integrated optics. However, it relies on the use of numerous associated chemical, thermal and etching steps. Moreover, it remains largely a surface processing technique and requires tedious cycles to produce 3-dimensional devices. In the last decade, direct femtosecond laser writing has emerged as an alternative technique for microfabrication inside transparent materials. Focused to small focal spots, intense light pulses make possible to form microscale 3-D optical elements [4, 67, 2, 68].

There are unique advantages in favor of the use of tightly focused femtosecond pulses. First, multiphoton ionization creates a modest density of free-carriers ($N_e \sim 10^{20}$ cm^{-3}) that can be controlled with the pulse duration [7]. Second, the nonlinear nature of the laser energy deposition mechanisms confines any subsequent material change to the focal volume [69]. Third, the pulse power, P, is maintained below or near the critical power for self-focusing ($P_C \sim 2.6$ MW in SiO$_2$). Even in those cases where $P > P_C$, beam depletion lowers the power long before the focal region. This is confirmed by the absence of self-phase modulation in the transmitted spectrum [7]. As a result, the pulse is not unstable to fluctuations. Taken together, the interaction process becomes extraordinary controllable and repeatable.

This change is connected with a changed refractive index. A lowered band gap, that we observed through a highly nonlinear response, discussed in the previous section, implies a higher refractive index. Experiments shown $\Delta n \sim 10^{-3}$. The same process is used for 3-dymantional wave guide writing [4, 67, 66].

In this section we explore the change in the effective refractive index associated with the modification in the regime of high laser fluency. As we shall see, the modification forms progressively a thick micro-lens inside all bulk materials we have investigated: fused and crystalline quartz, LiF, BK7, sapphire, mica. The defocusing of the lens implies a large decrease of the refractive index that can be achieved by nano-scale material disruptions (nano-cracking).

We concentrate our study on fused silica in which the modification takes the form of an array of planar nano-cracks [70, 37]. These arrays are characterized by their form birefringence [70, 71]. We study the nano-scale material rearrangement that is perfected shot after shot. We demonstrate that as the void inclusions grow throughout the breakdown region, a 2% refractive index decrease is reached without increasing linear absorption or scattering. This makes the approach suitable for building advanced, high contrast 3D-optical devices in bulk materials.

In the experiments, we use 130 fs laser pulses with peak energy up to few hundred nJ at $\lambda_{las} = 800$ nm. With our NA = 0.65 microscope objective, we would reach a peak intensity $I_0 = 3 \times 10^{14}$ W cm^{-2} and peak power $P_0 = 2 \times 10^6$ W if the focus were in vacuum. The threshold intensity for non-linear absorption is $I_{th} \cong 1.2 \times 10^{13}$ W cm^{-2} in fused silica [19]. The focus is placed 75 microns under the surface so that the light intensity remains low on the surface and spherical aberrations do not affect our focal spot. Figure 5.5 shows the cross-sectional morphology of modified SiO_2 after irradiations with different number of linearly polarized pulses. The modification progressively assumes the shape of a bi-convex micro-lens, determined by the intensity distribution in the focal volume. The size of the lens is controlled by the laser exposure. The SEM image reveals that the local change in the material optical properties is caused by the formation of a self-organized array of nano-planes that have been identified as void nano-cracks ($\cong$ 10 nm wide) [72, 71]. These stretch through the breakdown region in planes that have their normal along the laser field direction. The sub-wavelength periodic structure ($\cong$ 250 nm spacing) is then accompanied by birefringence and a lower refractive index.

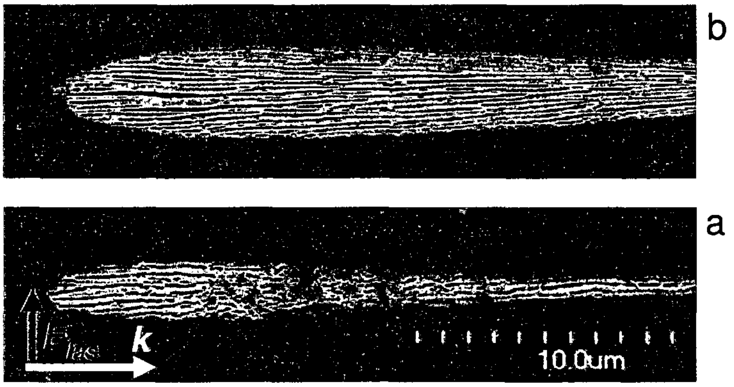

Figure 5.5: Cross-sectional images of the modified regions in fused silica. The modifications were done by repeatedly illuminating bulk materials with 10^2 (a) and 10^5 (b) focused pulses at 350 nJ. Samples are cleaved and etched (1% HF) to reveal the presence of nano-cracks in bulk by SEM imaging. The relative position of images in the k-direction is arbitrary.

We can estimate the average refractive index modification in the modified region by measuring the change in divergence of a low intensity beam that passes through it. The measurement of the beam divergence after modification of fused silica is shown in figure 5.6. Experimentally we use a second, higher numerical aperture (NA = 0.75) microscope objective to collect and collimate the light transmitted through the sample. We focus ($f_{lens} = 50$ mm) the collimated beam on a CCD. As we translate the imaging system along the optical axis, we measure the changes in the size (FWHM) of the Gaussian beam on the CCD. This measures the beam divergence. The top curve in figure 5.6 corresponds to the response of the fresh material. The bottom curve was obtained when the material was previously exposed to 10^7 laser shots at 350 nJ. The divergence decreases for the beam propagating through a modified region. We estimate that the waist increases by a factor of five, compared with the beam focused on a fresh spot. According to the bi-convex shape of the modification, the large defocusing is associated with a large decrease of the refractive index.

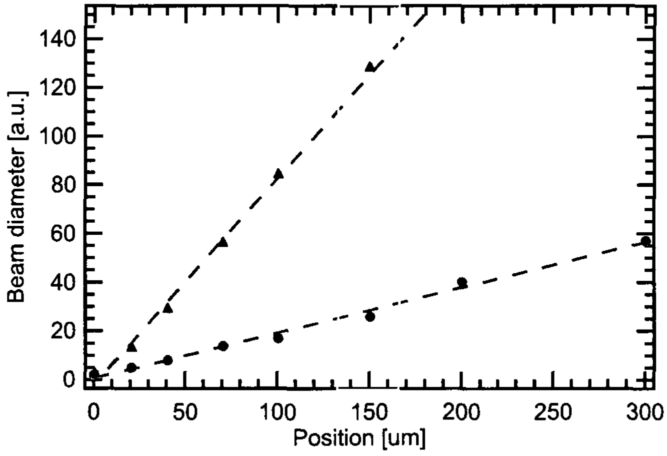

Figure 5.6: Measurement of the divergence of the laser beam passing through fresh (triangles) and modified materials (circles) with 10^7 shots laser shots at 350 nJ. The defocusing power of the embedded lens leads to a decrease of the beam divergence by a factor 5.

Form birefringence arises because of the anisotropic ordered arrangement of transparent materials on a scale smaller than the wavelength. Considering the idealized case of infinite periodic planar void cracks (thickness t_1) in fused silica (thickness t_2), the treatment of the form birefringence problem shows that the structure behaves like a uniaxial crystal where n_p (resp. n_s) is the effective index for an incident field perpendicular (resp. parallel) to the planes [73]. If $n = 1.45$, $t_1 = 8$ nm, $t_2 = 200$ nm that is $R = t_1/t_2 = 4\%$, all typical numbers from figure 5.5, we obtain $n_p = n\sqrt{(R+1)/(Rn^2+1)} \cong 1.42$ and $n_s = n\sqrt{(R/n^2+1)/(R+1)} \cong 1.435$. The formation of the cracks with sub-wavelength periodicity should therefore be accompanied by a polarization dependent-decrease of the refractive index exceeding 2%.

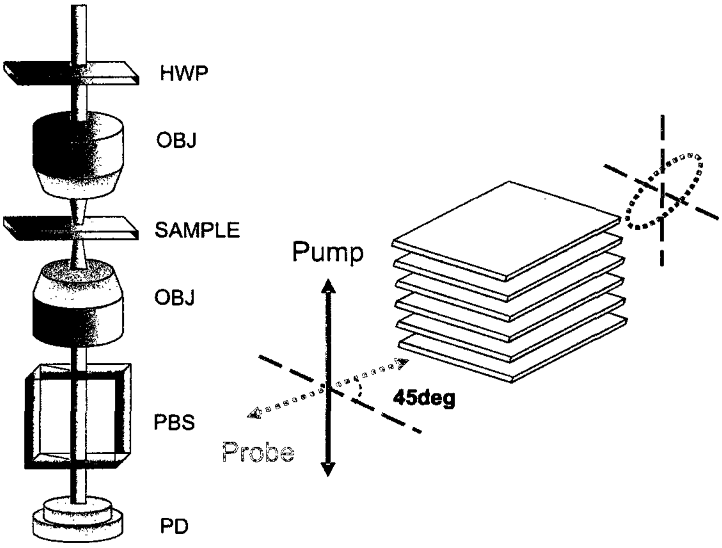

Figure 5.7: The pump and the probe light correspond to the same laser beam at different intensities. The polarization of the probe is rotated by 45 relative to the pump using a half-wave-plate (HWP). The form birefringence of the micro-lens changes the probe polarization from linear to elliptical and further(left panel). The probe polarization state is fully characterized by a rotating polarizer (PBS) and a photo-diode (PD).

We measure form birefringence in fused SiO_2 using a low intensity probe linearly polarized at 45 relative to the writing laser polarization (p) as shown schematically in Fig. 5.7. By analyzing the polarization state of the transmitted beam, we obtain, the phase delay between $p-$ and $s-$ polarized light, $\Delta\phi$, as a function of the number of shots (5.8). We find that the polarization changes gradually from linear to circular as the number of shots of the writing laser increases. Accordingly, over the $d \cong 25\mu$m long interaction region, the phase delay exceeds that of a quarter-wave plate for a 10^7 shot exposure. It corresponds to a polarization sensitivity of the refractive index $\Delta n = n_p - n_s = \Delta\phi\lambda_{las}/2\pi d \cong 1\%$ which is in reasonable agreement with our form birefringence predictions (see above).

Based on the birefringence properties, one would expect also a polarization dependence in the power of the lens. However, the phase advance

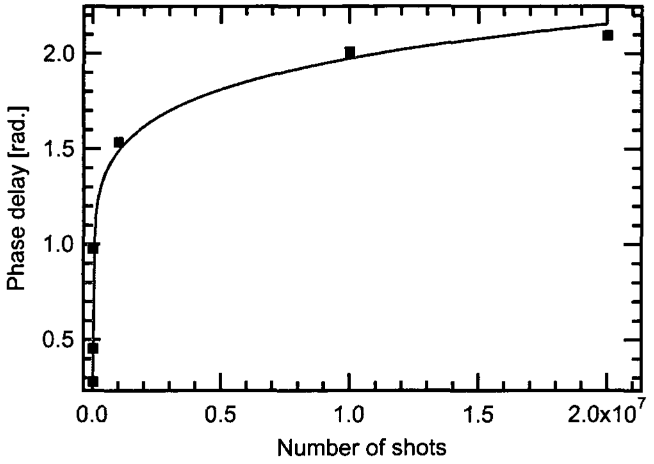

Figure 5.8: Phase delay $\Delta\phi = 2\pi(n_p - n_s)d/\lambda_{las}$ measured between $p-$ and $s-$ polarized light propagating trough the modified material. The measurements are performed after modification of SiO_2 with different number of laser shots ($E = 350$ nJ). The growth of birefringence correlates with the sub-wavelength periodic arrangement of materials that grows and is perfected (fig. 5.5) on a shot-to-shot basis.

implied by this self-generated lens is much greater than the relative phase advance of $s-$ and $p-$ polarized light. Accordingly, we observe very little difference between polarizations when we characterize the large defocusing power of the lens (as in fig. 5.6).

Nevertheless, we can probe the self-formed lens spatially by performing a $z-$scan of the refraction properties of the modified region for $p-$ (writing) and $s-$ polarized light. As shown in Fig. 5.9, we focus the low intensity probe light with the microscope objective inside the modified region and measure the energy in the central region of the transmitted beam, using an on-axis aperture. The size of the aperture is set to transmit 40% of the laser beam, when it propagates through a fresh material. This provides for the optimim sensitivity of the z-scan. Translating the focusing objective along the optical axis changes the beam divergence and, therefore, the signal amplitude on the photodiode. Using this approach we can separate between the influences of the back and the front surfaces of the lens.

Figure 5.10 shows the measured signal as a function of the probe position for a lens written with 10^7 shots at 350 nJ. The zero position corresponds to the probe beam focusing exactly at the same location as the writing beam. The intensity measured in this situation is much larger than that measured

.

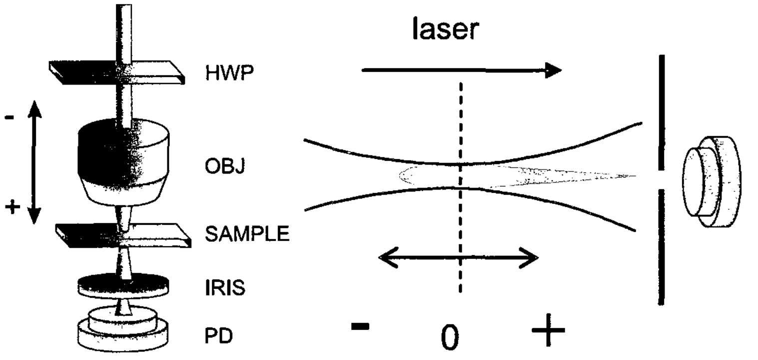

Figure 5.9: The schematics of the $z-$ scan experiment. As the microscope objective (OBJ) focus is translated along the micro-lens (right panel) in the sample, the beam divergence and the transmission through an on-axis aperture change. The laser field polarization is controlled by the half-wave-plate (HWP) and the signal is collected by a photo-diode (PD).

.

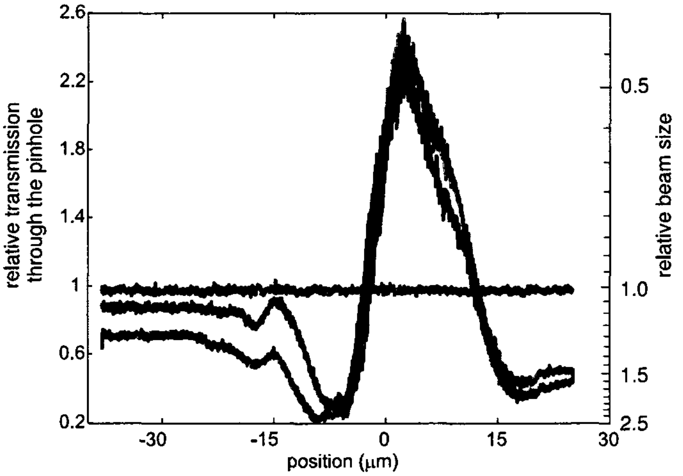

Figure 5.10: $z-$ scan of the refraction properties of the modified structure using $p-$ (red) and $s-$ (blue) polarized probes. The spot size, or divergence, of the probe beam (right ordinate) is directly evaluated by measuring the probe energy transmitted by an on-axis aperture (left ordinate). Signal level 1 corresponds to 40% transmission by the apperture of the probe beam passing through a fresh material (green). The measurement shows a polarization dependent refraction at the first interface of the structure.

for an unmodified material (black - unity level). This is a clear evidence of a decrease in divergence.

By moving the probe focus progressively toward the front-curvature of the lens (positive values), the signal becomes lower than unity when the beam waist crosses the first principal plane H1 of the formed lens. In fused silica, the full scan measurement (fig. 5.10) shows that form birefringence is present at the input interface of the modified region. As we move closer to the front of the lens, the measured signal becomes highly polarization dependent. A stronger refraction occurs for the writing polarization, p, as predicted by our calculations and birefringence measurements. The polarization sensitivity vanishes with the sharp exit tip where the number of nano-planes drops to only a few (scan toward negative $z-$ positions).

The creation of the defocusing microlens in the interaction region in fused silica does not necessary require the formation of a birefringent structure. We found that similar divergence change is achieved when circularly polarized light is used for lens writing. In this case the overall shape of the modification is bi-convex, as with the linearly polarized light. However, the nano-cracks are quasi-random in shapes and location [74, 75]. In general the creation of multiple sub-wavelength size voids inside the bulk leads to the reduction of the volume refractive index, $\Delta n \approx R \times (1 - n)$ (*e.g.* $\Delta n \approx -0.02$, for $R = 5\%$ (volume fill ratio) and $n = 1.45$). We repeated the lens writing experiment in other transparent dielectrics (crystal SiO_2, BK7, LiF, sapphire and mica), using the same experimental conditions as for fused SiO_2. We found similar increase in the signal through an on-axis aperture, (by a factor of 1.5 to 2) in all of them. Although the formation of the birefringent structures has not yet been reported for other dielectrics, this divergence decrease implies that nano-voids are indeed created in each case. This shows that defocusing lens self-formation is likely to be a general phenomenon for dielectrics.

The refractive index change and the birefringence increase that we obtain in fused silica are very large. They can be induced anywhere in 3D space with minimal material transport. The results emphasize that efficient polarization-dependent component such as wave-plates, retarders and couplers can be efficiently fabricated in bulk fused silica provided that the ordered and self-limited material rearrangement occurs on a scale much smaller than the component size. This is achieved without any noticeable increase in linear absorption. These capabilities open a new route to integrating advanced functionality inside optical fibers or bulk materials.

While we concentrated in this work on the micro-lens self-formation and its potential technological benefits, the underlying material science is partially understood. One tool to understanding and monitoring material modification in real time is to look at the non-linear absorption of each individual pulse that creates the structure. In the next section we will focus on this aspect.

5.3 Enhanced Transmission

Until this point all parts of this thesis have been published or submitted for publications. The rest of the thesis summarizes unpublished observations.

As we have shown in the last section, the repeated laser breakdown inside the focal volume of transparent dielectric slab, such as fused silica, crystalline quartz or others creates microscopic material modification leading to the formation of the defocusing micro-lens. The lens provides a feedback to the refraction of the laser beam that has created it. The location of the micro-lens is in the half-plane before the laser focus, where laser energy is deposited through multi-photon ionization process, and this leads to strong reduction in the beam divergence.

It is reasonable to expect that the gradual material restructuring and the changes in the laser intensity distribution at the focal region must influence the process of multi-photon ionization for the subsequent laser shots. Moreover, the creation of nanoscale voids inside the micro-lens volume cause strong changes in the local electric field distribution on the boundary of these voids with the dielectric bulk.

The ionization of wide band gap dielectrics with femtosecond laser pulses depends exponentially on the laser intensity [8]. Therefore, the formation of the micro-lens in the interaction region will result in the changes to the ionization probability. We can monitor the ionization yield through nonlinear absorption [7] during the process of the formation of the lens.

We use 800 nm 130 fs laser pulses with energy of 350 nJ. We use NA = 0.65 microscope objective, the focus is placed 75 microns below the surface so that the light intensity remains low on the surface and spherical aberrations do not affect our focal spot. We use an integrating sphere to measure the transmitted light. These experimental conditions are identical to those used for the writing of the micro-lens in fused silica (Fig. 5.5).

In Fig. 5.11 we show the nonlinear transmission as a function of the number of laser shots at the same spot in the sample, where the first shot was made at a fresh spot. The transmission decreases first due to the reduction in the material band gap resulting from the rearrangement in SiO_2 rings inside fused silica. This is the nonlinear memory effect also shown in Fig. 5.1 and 5.2.

When the number of laser shots increases further, the transmission starts growing. This is the signature of the micro-lens formation and its effect on the ionization efficiency. Over 10^6 laser shots the transmission increases by $\sim$15%. As in the case of the nonlinear memory in fused silica the change in

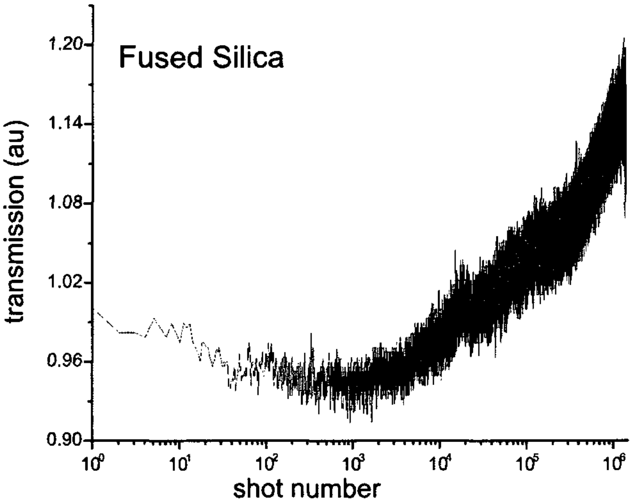

Figure 5.11: Nonlinear transmission as a function of the number of shots for fused silica. 800 nm, 130 fs, 350 nJ laser pulses; NA = 0.65 microscope objective. Transmission normalized to the first shot value measured at the fresh sample.

nonlinear transission at high laser pulse energies (Fig. 5.2) occurs due to the changes in the absorption threshold Fig. 5.1. We now verify that the increase in transmission at high input laser pulse energies, due to the formation of the micro-lens in fused silica, is accompanied by an increase in the absorption threshold enegry.

In Fig. 5.12 we show the transmission as a function of the input laser pulse energy for fused silica. The two curves correspond to the two different sample conditions. In both cases the material was illuminated at the same spot, while the laser input pulse energy was ramped from $\leq$ 10 nJ up to 350 nJ. In the first case, the bottom green curve, fresh sample was used for the the first laser shot. In this case the nonlinear absorption threshold occurs at ~30 nJ. In the second experiment, the top red curve, the sample was previously illuminated with 10^7 laser shots at 350 nJ, forming the defocusing micro-lens. Here the pulse energy required for the nonlinear absorption is ~90 nJ.

From Fig. 5.12 we see that the formation of the micro-lens results in higher transmission at all intensities above the breakdown threshold of pristine material. After modification it takes 3 times more energetic laser pulses to start the ionization, compared with fresh fused silica. We also find that the linear transmission through the modified region, measured at low laser intensities, remains at the level of 96% compared with the fresh sample.

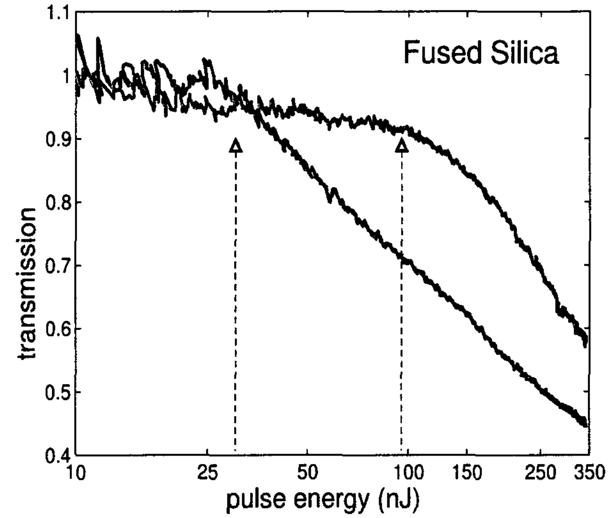

Figure 5.12: Nonlinear transmission for fresh (bottom green) and modified (top red) fused silica. The modification (writing) was done with 10^7 laser shots at 350nJ. The arrows point to the breakdown threshold values in the two cases.

We have observed similar increases in the ionization threshold in all transparent dielectrics we have investigated (fused and crystalline SiO_2, Al_2O_3, LiF, BK7, mica and Er-doped phosphate glass). The results for quartz and LiF are shown in Fig. 5.13. In all cases shown in Fig. 5.12 and 5.13, the micro-lens writing was done with the identical laser pulse parameters. The resulting micro-lenses may be different in their size and the effective refractive index change for different sample materials. Therefore the magnitude of the enhanced transmission is also different.

We apply numerical models to fit the transmission results for fused silica presented in Fig. 5.12. We use $\sigma_6 = 4 \times 10^{13}$ (TW cm^{-2})$^{-6}$cm^{-3}ps^{-1} for fresh sample and $\sigma_6 = 1.6 \times 10^{14}$ (TW cm^{-2})$^{-6}$cm^{-3}ps^{-1} for the modified sample. The same σ_6 values were used for the nonlinear memory analysis. The avalanche coefficient is set to $\alpha = 0.1$ J^{-1}cm^2.

In order to evaluate the change in the laser intensity under the conditions of the enhanced transmission, we change the waist size at the focus. Good agreement between the theory and the experiment is observed when the $1/e$ radius is 0.4 μm for the fresh material and 1 μm with the micro-lens. The increase of 2.5 times in the waist size corresponds to 6.25 times decrease in laser intensity.

The micro-lens formed in fused silica is built up by parallel void planes. This structure exhibits strong birefringent properties as shown in Fig. 5.8 and

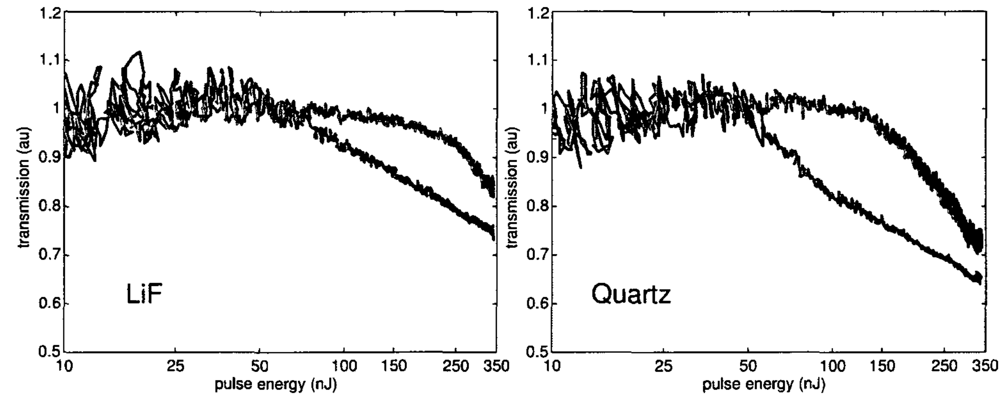

Figure 5.13: Nonlinear transmission for fresh (bottom green) and modified (top red) LiF (left pane) and crystalline Quartz (right pane). The modification (writing) was done with 10^7 laser shots at 350nJ.

5.10. As a result, enhanced transmission should be polarization sensitive. For the laser light polarized orthogonally to the writing laser polarization, the effective refractive index change inside the modified region is approximately half. This difference in refractive index should translate linearly into the refractive power of the lens. Therefore, the expected intensity change for the orthogonal polarization is only 1.5 times greater than in the case of the fresh material.

In Fig. 5.14 we show the change in transmission when the laser polarization is rotated by 90° (dotted blue curve), relative to the writing polarization (solid red curve). The apparent ionization threshold in this case is even lower than in the fresh material. This is the signature of the material band gap reduction at the initial stages of the ionization. The same threshold change is shown in Fig. 5.1.

The big difference between the two polarization states implies that the mechanism behind enhanced transmission is not solely the micro-lens defocusing. On the input surface of the micro-lens we do not yet understand what other effects are important. To gain insight we concentrate on the spatial properties of the transmitted beam.

The enhanced transmission effect and the divergence decrease due to the formation of the micro-lens are both related to the formation of the nanocracks inside the bulk. It is important to establish whether these effects are related through linear diffraction or nonlinear propagation and ionization. We have compared the divergence of the beam at low pulse energy, corresponding to linear propagation, and at high energy, above the breakdown threshold. We measured the spatial profile of the transmitted beam in the

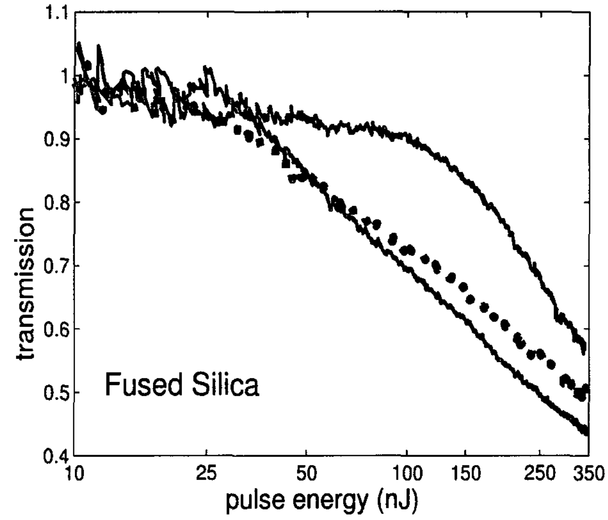

Figure 5.14: Nonlinear transmission for fresh (bottom green) and modified (top red) fused silica. Laser polarization orthogonal to the writing polarization (dotted blue). The modification (writing) was done with 10^7 laser shots at 350nJ.

far field, imaged on the CCD. The line cuts through the image for two laser input pulse energies are shown in Fig. 5.15.

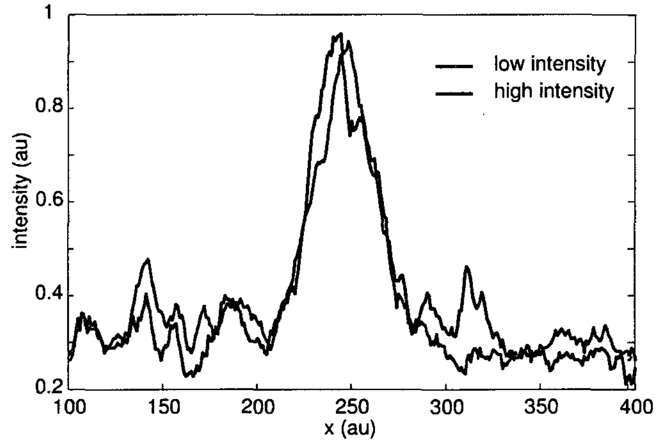

Figure 5.15: Far field intensity profile for low (blue) and high (red) laser intensities, after propagation through the microlens. The modification (writing) was done with 10^7 laser shots at 350nJ.

From Fig. 5.15 we see that the divergence remains the same for low and high intensities inside the focal volume. Therefore, enhanced transmission is not determined by nonlinear interaction with the micro-lens structure in the focal volume. The local laser field distribution around the nano-cracks is not modified by plasma formation.

We do not fully understand the transmission results yet. If it is caused by the micro-lens redirecting the beam, why is the transmission so polarization sensitive? If it is caused by the free carriers that we inject, why does the beam profile in the far field remains the same at intensities below and above ionization threshold? If it is caused by an increase in the ability of the material to withstand high intensities, purification, why is the threshold so low for orthogonal polarization?

5.4 SHG in Quartz

To gain additional insight, we changed our emphasis from fused SiO_2 to crystal quartz and from measuring the transmission of the fundamental beam, to measuring the second harmonic. We found that, in addition to the formation of the defocusing micro-lens, the repeated ionization by femtosecond laser pulses results in the self-formation of favorable phase-matching for the second harmonic generation with the conversion power efficiency of $\eta = P_{400}/P_{800}^2 \approx 10^{-6}$.

We used 800 nm 50 fs pulses focused $\sim 150\mu$m inside 1 mm thick z-cut quartz sample with microscope objective (numerical aperture NA = 0.25). The pulse energies were below 400 nJ (intensity 9×10^{13} W cm^{-2} if the focus were in vacuum). The transmitted light was collimated using a second objective (NA = 0.25) and collected by a photo diode. We used an optical filter before the photo diode to block the fundamental 800 nm light and collect only the second harmonic emission. The results in Fig. 5.16 show how the second harmonic increases with the number of shots for different input pulse energies. The second harmonic signal is normalized in each case to the fundamental pulse energy, which allows the direct comparison of the second harmonic efficiency. It is clear from Fig. 5.16 that for the highest conversion efficiency, lower pulse energies should be used. However, for the maximum SGH signal the highest available pulse energy is required.

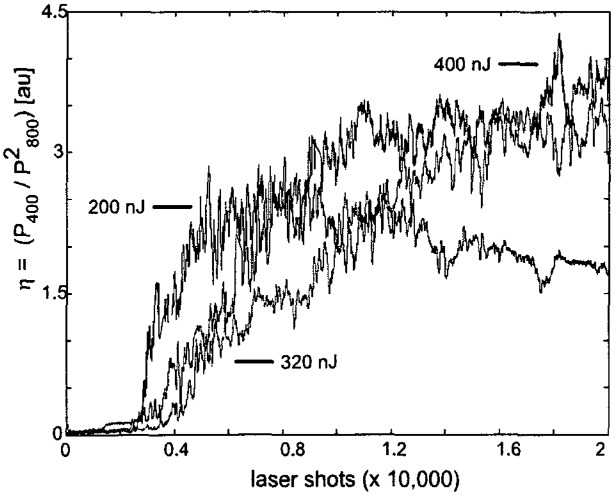

Figure 5.16: Second harmonic signal as a function of laser exposure for different incident laser pulse energies. New material was used at every first shot. The data was 30-points averaged.

The material modification that leads to the creation of efficient second harmonic generation is related with the enhanced transmission effect and micro-lens formation, discussed earlier. In Fig. 5.17 we show the comparison between the changes in the transmission of the 800 nm laser and the appearance of the SHG as a function of the number of shots. From the figure we see that the number of laser shots required for the SHG buildup is 10 times smaller than the number required for the start of the enhanced transmission.

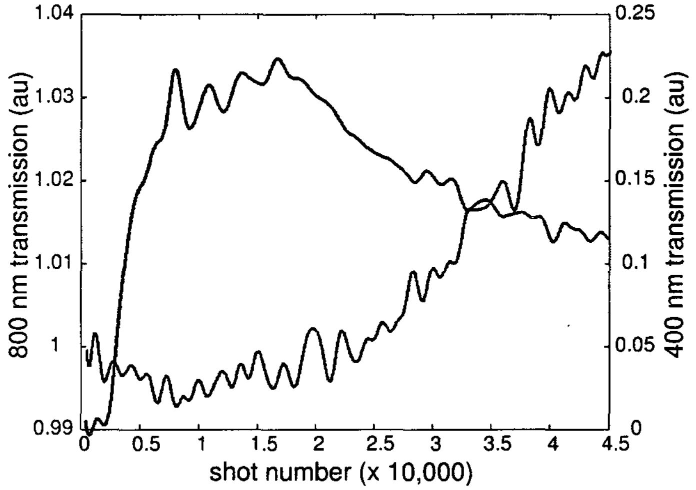

Figure 5.17: Fundamental and second harmonic signal as a function of the number of shots by 800 nm laser. Red - 800 nm, blue - 400 nm, fresh material at the first shot. Noise filtered for clarity.

Over the first ~ 20000 shots, the SHG reaches its peak value. For this number of shots the transmission of the fundamental is not modified (see Fig. 5.17). We compare the breakdown transmission as a function of the laser pulse energy for the 800 nm laser for the fresh material and after the total of 24000 shots. The results are shown in Fig. 5.18. The two transmission curves, in dark and light red, corresponding to fresh and previously ionized samples correspondingly, overlap. This indicates that the breakdown threshold for the quartz sample is not modified after 24000 shots.

The second harmonic signal increase is shown in Fig. 5.18 with blue lines. The dark blue curve corresponds to the initial buildup of phase matching conditions for SHG that start at ~150 nJ. The light blue curve corresponds to the second harmonic memory and shows strong SHG signal at low pulse energies.

From Fig. 5.18 we find that material modification for the second harmonic generation phase matching is permanently written into the sample.

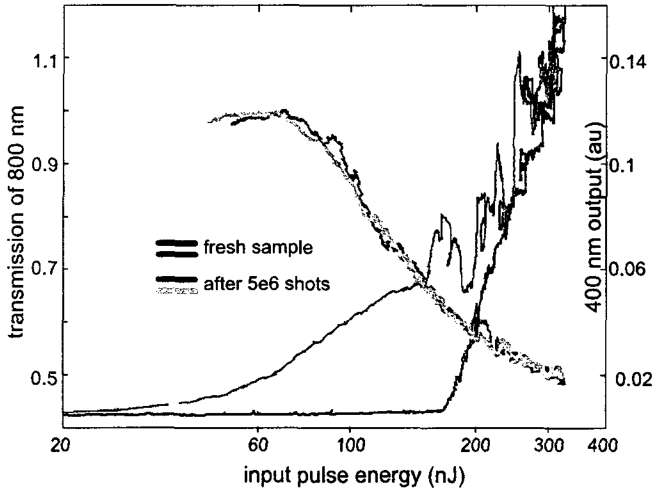

Figure 5.18: Fundamental (left ordinate) and SH (right ordinate) signal as a function of the input pulse energy. Darker curves (red - 800 nm, blue - 400 nm), fresh material at the first shot; Lighter curves (pink - 800 nm, cyan - 400 nm), after 24000 shots of varying laser pulse energy (up to 320 nJ). Back dashed line - parabolic fit.

The second harmonic generation occurs at pulse energies well below the ionization threshold. This is an indication that the observed second harmonic generation is not transient effect in ionization, but is a $\chi^(2)$ phenomenon. This is also clearly seen from a quadratic dependency of the SHG signal on the input pulse energy.

The measurements presented so far were done with the same laser polarization orientation relative to the crystal lattice. However, the efficiency of the second harmonic buildup depends on the incident laser polarization. In Fig. 5.19 we present the results for 210 nJ input pulse energy for different linear polarization orientations of the fundamental laser field. The 0 degrees angle corresponds to $\phi_0 = 0$ relative to the quartz $\hat{x}$ axis. The efficiency of the second harmonic buildup varies by more than 3 times along different directions in the lattice. The observed angular dependence does not change with the number of laser shots.

α-Quartz crystal has a non-zero $\chi^{(2)}$ tensor. However, the strength of the total second harmonic signal should remain constant for any alignment angle between the laser linear polarization and the z-cut crystal $\hat{x}$ axis. Our observation of the modulation in the second harmonic signal with the azimuthal angle, implies that the phase matching conditions are built preferentially for the $\hat{y}$ direction in the crystal.

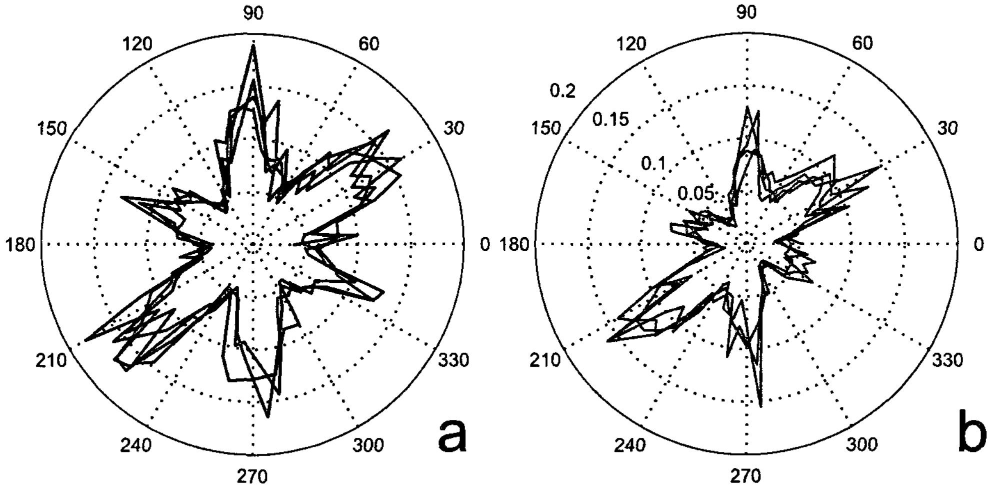

Figure 5.19: Second harmonic signal as a function of laser polarization direction. New material was used at every first shot. Laser input pulse energy 210 nJ. The data was 30-points averaged. (a) second harmonic signal maximum between 500 — 2450 shots. (a) SHG averaged between 45000 — 49500 shots

The preferential azimuthal angles for the second harmonic buildup shown in Fig. 5.19 may be related to the nonuniform absorption of the fundamental 800 nm light as shown in Fig.4.1. There the phase of the $\pi/2$ - periodic modulation in the absorption of the fundamental pulse is defined by the residual birefringence of the peripheral beams and depends on the specific current alignment of the optical components in the experiment. The phase of this modulation with respect to the lattice orientation may vary between different experiments.

To check whether the same random phase is observed in the second harmonic memory buildup, we have repeated the same experiment as in Fig. 5.19. We found that the shape and the absolute phase of the second harmonic generation peaks are not preserved. The new results (central part in Fig. 5.20) also exhibit strong azimuthal variation, but now the maximum second harmonic generation occurs at 15 and 195 deg relative to the crystal $\hat{x}$ axis.

We have established, that the efficiency of the second harmonic buildup depends on the polarization of the fundamental beam relative to the crystal axis. We will now probe the second harmonic conversion properties of the written modification by using a weak probe. For all the different polarizations of the fundamental, used to "write-in" the second harmonic memory, we will measure the second harmonic generation produced with a weak probe at the intensity below the ionization threshold. We measure the second harmonic signal for different polarizations of the probe. The results are presented in Fig. 5.20.

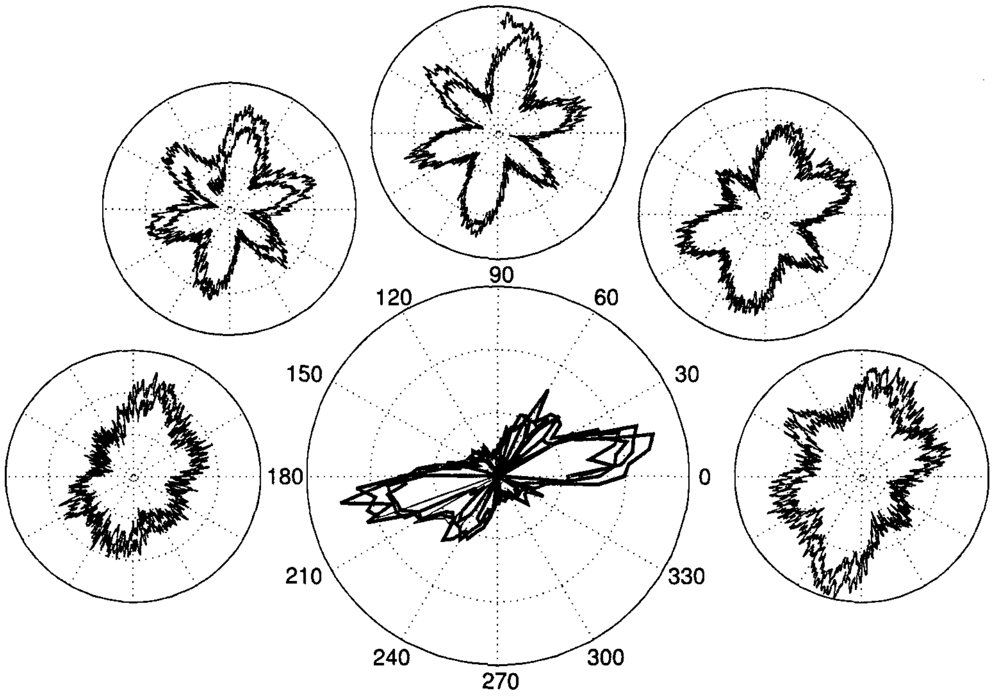

Figure 5.20: (centre) The efficiency of second harmonic, produced by the 800nm pump pulse, as a function of its polarization orientation, 0 deg correspond to $\hat{x}$ axis of the crystal. The peripheral polar plots are located at 0, 45, 90, 135 and 180 deg, indicating the pump laser polarization orientation. They show the second harmonic, produced by the probe pulse, as a function of its polarization angle.

Figure 5.20 shows both the efficiency of the second harmonic buildup as a function of the laser polarization (shown in the central polar plot) and the efficiency of second harmonic generation for the weak probe (shown in the peripheral polar plots). These are located at the angles of 0, 45, 90, 135 and 180 degrees, indicating the orientation of the pump polarization that was used to "write-in" the modification in the material. Second harmonic signals from both the pump and the probe are modulated and depend strongly on the laser polarization. From the orientation of the curves in Fig. 5.20 we find that the their modulation is 60 deg out of phase with respect to each other. In addition the modulation amplitude of the probe second harmonic generation varies between different orientations of the pump.

The results presented in Fig. 5.19 and Fig. 5.20 indicate a relationship between the crystal lattice structure and the laser polarization leading to different phase matching properties of the the modification induced in the material. Using both the fundamental laser pulse and its second harmonic can provide an efficient way to control the modification properties and build an efficient SHG converter.

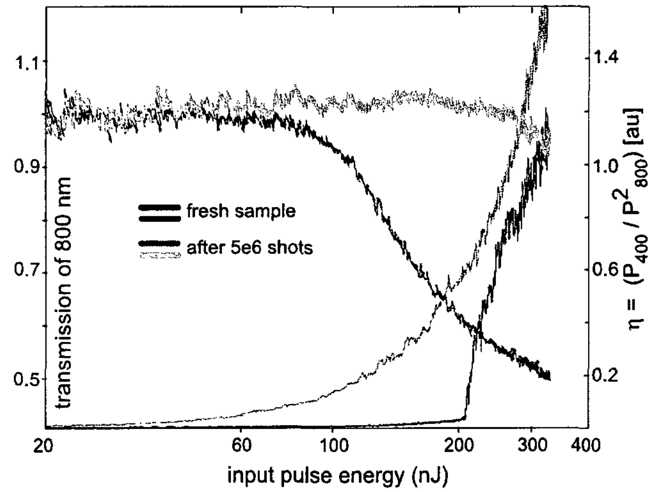

Figure 5.21: Fundamental (left ordinate) and second harmonic (right ordinate) signal as a function of the input pulse energy. Darker curves (red - 800 nm, blue - 400 nm), fresh material at the first shot; Lighter curves (pink - 800 nm, cyan - 400 nm), after ~ 5×10^6 shots at 320 nJ input laser pulse energy.

After ~ 5×10^6 laser shots at the same spot, a defocusing micro-lens is formed in the interaction region [20]. The creation of the micro-lens is followed by an enhanced transmission. As a result, the second harmonic is also enhanced. The second harmonic and the fundamental laser transmission as a function of the input pulse energy for the fresh material and for the material previously modified by ~ 5×10^6 laser shots at 320 nJ is shown in Fig. 5.21.

We can estimate the maximum second harmonic generation efficiency for pristine z-cut quartz sample, assuming optimal focusing [76]. For our experimental conditions and taking into account 400 nm and 800 nm phase mismatch, the conversion efficiency $\eta = P_{400}/P_{800}^2 \approx 1 \times 10^{-14}$, where P measured in Watt. Our experiments show a much higher conversion efficiency of $\eta \sim 1 \times 10^{-6}$. This strong conversion efficiency in $\sim 30 \mu m^3$ volume, has a potential for many technological applications.

The formation of the micro-lens leads to the decrease in the 800 nm beam divergence, maintaining its Gaussian profile. The spatial distribution of the SHG consists of multiple peaks as shown in Fig. 5.22. The modification of the macroscopic refractive index in the ionization volume leads to the changes in the laser propagation mode. The fundamental mode remains Gaussian (or TEM_{00}), however the SHG corresponds to higher order mode such as TEM_{03}.

The mode change occurs due to the formation of planes through the interaction region, separated by λ in the material. These planes are revealed in the SEM image after polishing and etching the sample in 20% HF for ~ 2 minutes. It has not yet been shown whether these plains are voids, however, the strong change in the macroscopic refractive index implies the formation of voids [20].

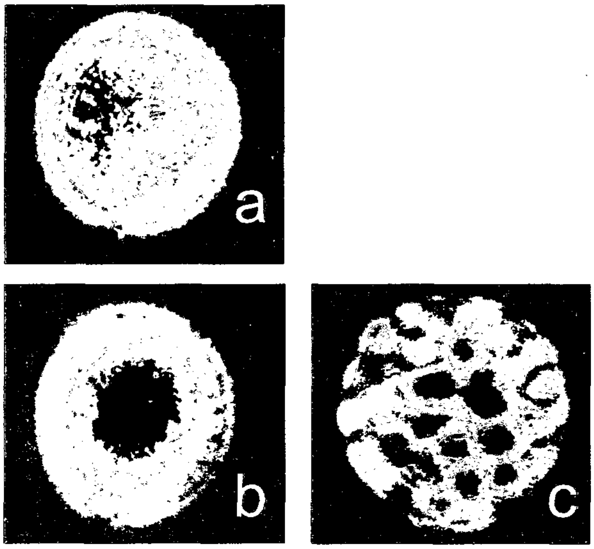

Figure 5.22: Low intensity fundamental (a, b) and second harmonic (c) far field spatial profile. a - fresh material; b,c - after $\sim 10^7$ shots at 500 nJ

Taken together, sections 5.3 and 5.4 show the potential of intense pulses to control all materials. This work is in its early stages, but it points to a new technology for optical materials. We have shown how large refractive index changes can be obtained and polarization elements can be fabricated to be used in optical components. We showed the creation of phased matched harmonics that can potentially store information in bulk materials.

To conclude this chapter, the use of femtosecond lasers to modify the material structure and the refractive index [4] of dielectrics has uncovered multiple unexpected phenomena. These include the formation of nano-pores inside the focal volume [2] and arranged planar nano-cracks [60, 37]. The nano-cracks follow laser polarization direction and its handedness [75]; they can be erased and written over [71]. The formation of structures in the focal volume is defined by several underlying physical effects: self-limiting nature of the interaction [7], nonlinear memory as a feedback to ionization by the laser field [19], creation of nano-plasmas accompanied with local field enhancements inside the bulk [77] and collision assisted strong field ionization [29].

The formation of nano-structures inside the focus is usually a many – laser shots process. The changes in the material structure induced by the ionization and the following relaxation, between the laser shots, affect both the band gap and the laser propagation and field distribution. The nano-cracks, self-formed after millions of laser shots into a bi-convex shape inside the focus [20], result in laser beam defocussing, and as a consequence a decrease in the nonlinear absorption, compared with the fresh material. In crystal quartz the material modification builds up to give rise to efficient second harmonic generation.

Chapter 6

Conclusion

We have presented the studies on the material ionization and modification with femtosecond laser pulses. This research work has resulted in several new insights into the physical mechanisms that occur during the interaction of intense laser fields with transparent dielectrics. In the studies of the material modification by femtosecond laser pulses, we have observed several new phenomena in the material restructuring.

We have shown a novel method for measurements of dielectric crystalline structure and provided the first experimental evidence for the dependence of the multi-photon ionization rates on the electronic band structure. The metrology can be extended to semiconductor materials using near infrared femtosecond laser sources. With ultrashort pulses the material damage due to ionization is so benign that the method can be used on biological samples.

We have shown the first ever measurements of the sub-laser-cycle dynamics in the material breakdown. The absorption of laser light is induced by the polarization of the injected conduction band electrons. The method provides a tool to probe experimentally the contributions of different absorption mechanisms, multi-photon ionization and avalanche. Extended to two colors, pump and probe experiments will provide a probe to the electron coherence time in solids.

We have first shown the experimental evidence for the field assisted avalanche ionization. From the increase in the avalanche rate for shorter laser pulses we have determined the presence of collision-assisted multi-photon ionization. Our model can be applied to dielectric surfaces where peak laser intensities are high and field-assisted avalanche dominates.

We have discovered the effect of nonlinear memory in dielectrics that provides a basis for the formation of nano-structures in wide band gap dielectrics. We have first shown the self-formation of the micro-lens inside the focal volume, induced by repeated multi-photon ionization. The strong birefringence and the defocusing power of the micro-lens can be utilized in a variety of the 3D photonic devices.

In work, still unpublished, we have observed experimentally enhanced transmission in all dielectrics. The increase in the breakdown threshold that follows the formation of the micro-lens, indicates a new observation of general physical phenomenon – the mitigation of dissipation.

In crystal quarts, we have discovered the self-formation of the favorable phase matching for the second harmonic generation that is being inscribed into the bulk. With the improved control over the modification properties, the process can be used to build frequency doubling devices in μm volume anywhere inside the bulk. To our knowledge neither enhanced transmission nor self-optimization of phase matching conditions have ever been observed before.

This research has improved our ability to measure and interpret the ionization process and the material properties of dielectrics. We can now observe subtle effects and we understand better the underlying physics. We believe this work will provide a basis for the future studies into ionization of solids and also will develop into variety of applications in microscopy and photonics.

Bibliography

[1] A. Marcinkevicius, S. Juodkazis, M. Watanabe, S. Matsuo, H. Misawa, and J. Nishii, "Femtosecond laser-assisted three-dimensional microfabrication in silica," *Opt. Lett.*, vol. 26, pp. 277–279, 2001.

[2] R. S. Taylor, C. Hnatovsky, E. Simova, D. M. Rayner, V. R. Bhardwaj, and P. B. Corkum, "Femtosecond laser fabrication of nanostructures in silica glass," *Opt. Lett.*, vol. 28, pp. 1043–1045, 2003.

[3] K. O. Hill, Y. Fujii, D. C. Johnson, and B. S. Kawasaki, "Photosensitivity in optical fiber waveguides: Application to reflection filter fabrication," *Appl. Phys. Lett.*, vol. 32, p. 647, 1978.

[4] K. M. Davis, K. Miura, N. Sugimoto, and K. Hirao, "Writing waveguides in glass with a femtosecond laser," *Opt. Lett.*, vol. 21, pp. 1729–1731, November 1996.

[5] P. Corkum and F. Krausz, "Attosecond science," *Nature Phys.*, vol. 3, p. 381, 2007.

[6] R. S. Taylor, C. Hnatovsky, E. Simova, D. M. Rayner, M. Mehandale, V. Bhardwaj, and P. B. Corkum, "Ultra-high resolution index of refraction profiles of femtosecond laser modified silica structures," *Opt. Express*, vol. 11, no. 7, pp. 775–781, 2003.

[7] D. M. Rayner, A. Naumov, and P. B. Corkum, "Ultrashort pulse nonlinear optical absorption in transparent media," *Opt. Exp.*, vol. 13, pp. 3208–3217, 2005.

[8] L. V. Keldysh, "Ionization in the field of a strong electromagnetic wave," *JETP*, vol. 20, p. 1307, 1965.

[9] L. Sudrie, A. Couairon, M. Franco, B. Lamouroux, B. Prade, S. Tzortzakis, and A. Mysyrowicz, "Femtosecond laser-induced damage and filamentary propagation in fused silica," *Phys. Rev. Lett.*, vol. 89, p. 186601, 2002.

[10] B. Walker, B. Sheehy, L. F. DiMauro, P. Agostini, K. J. Schafer, and K. C. Kulander, "Precision measurement of strong field double ionization of helium," *Phys. Rev. Lett.*, vol. 73, pp. 1227–1230, 1994.

[11] G. L. Yudin, L. N. Gaier, M. Lein, P. L. Knight, P. B. Corkum, and M. Y. Ivanov, "Hole-assisted energy deposition in clusters and dielectrics in multiphoton regime," *Laser Phys.*, vol. 14, pp. 51–56, 2004.

[12] M. Gertsvolf, P. P. Rajeev, D. M. Rayner, and P. B. Corkum, "Measuring attosecond ionization dynamics inside dielectrics," in *CLEO/QELS*, 2007.

[13] M. Gertsvolf, M. Spanner, D. M. Rayner, and P. B. Corkum, "Attosecond metrology in solids," *Phys. Rev. Lett.*, vol. submitted, 2009.

[14] J. Muth-Böhm, A. Becker, and F. H. M. Faisal, "Suppressed molecular ionization for a class of diatomics in intense femtosecond laser fields," *Phys. Rev. Lett.*, vol. 85, pp. 2280–2283, Sep 2000.

[15] I. V. Litvinyuk, K. F. Lee, P. W. Dooley, D. M. Rayner, D. M. Villeneuve, and P. B. Corkum, "Alignment-dependent strong field ionization of molecules," *Phys. Rev. Lett.*, vol. 90, p. 233003, 2003.

[16] D. Pavicic, K. F. Lee, D. M. Rayner, P. B. Corkum, and D. M. Villeneuve, "Direct measurement of the angular dependence of ionization for n2, o2 and co2 in intense laser fields," *Phys. Rev. Lett.*, vol. 98, p. 243001, 2007.

[17] N. Mairesse, Y. andDudovich, J. Levesque, M. Y. Ivanov, P. B. Corkum, and D. M. Villeneuve, "Electron wavepacket control with elliptically polarized laser light in high harmonic generation from aligned molecules," *New J. Phys*, vol. 10, p. 025015, 2008.

[18] V. R. Bhardwaj, D. M. Rayner, D. M. Villeneuve, and P. B. Corkum, "Quantum interference in double ionization and fragmentation of $c6h6$ in intense laser fields," *Phys. Rev. Lett.*, vol. 87, p. 253003, Nov 2001.

[19] P. P. Rajeev, M. Gertsvolf, E. Simova, C. Hnatovsky, R. S. Taylor, V. R. Bhardwaj, D. M. Rayner, and P. B. Corkum, "Memory in nonlinear ionization of transparent solids," *Phys. Rev. Lett*, vol. 97, p. 253001, 2006.

[20] D. Grojo, M. Gertsvolf, H. Jean-Ruel, S. Lei, L. Ramunno, D. M. Rayner, and P. B. Corkum, "Self-controlled formation of micro-lenses

by optical breakdown inside wide-band-gap materials," *Appl.Phys. Lett.*, vol. 93, p. 243118, 2008.

[21] A. Perelomov, V. Popov, and M. Terentev, "Ionization of atoms in alternating electric field," *Sov. Phys. JETP*, vol. 23, p. 924, 1966.

[22] M. Ammosov, N. Delone, and V. Krainov, "Tunnel ionization of complex atoms and of atomic ions in an alternating electromagnetic field," *JETP*, vol. 91, p. 2008, 1986.

[23] T. Siedeman, M. Y. Ivanov, and P. B. Corkum, "Role of electron localization in intense-field molecular ionization," *Phys. Rev. Lett.*, vol. 75, pp. 2819–2822, 1995.

[24] P. B. Corkum, "Plasma perspective on strong-field multiphoton ionization," *Phys. Rev. Lett.*, vol. 71, pp. 1994–1997, 1993.

[25] M. Lenzner, L. J. Kruger, S. Sartania, Z. Cheng, C. Spielmann, L. G. Mourou, W. Kautek, and F. Krausz, "Femtosecond optical breakdown in dielectrics," *Phys. Rev. Lett.*, vol. 80, pp. 4076–9, 1998.

[26] P. Martin, S. Guizard, D. P., G. Petite, P. d'Oliveira, P. Meynadier, and M. Perdix, "Subpicosecond study of carrier trapping dynamics in wide-band-gap crystals," *Phys. Rev. B*, vol. 55, p. 5799, 1997.

[27] F. Qur, S. Guizard, and P. Martin, "Time-resolved study of laser-induced breakdown in dielectrics," *Europhys. Lett.,*, vol. 56, pp. 138–144, 2001.

[28] M. Gertsvolf, H. Jean-Ruel, P. P. Rajeev, D. Klug, D. M. Rayner, and P. B. Corkum, "Orientation-dependent multiphoton ionization in wide band gap crystals," *Phys. Rev. Lett.*, vol. 101, p. 243001, 2008.

[29] P. P. Rajeev, M. Gertsvolf, P. B. Corkum, and D. M. Rayner, "Field dependent avalanche ionization rates in dielectrics," *Phys. Rev. Lett.*, vol. 102, p. 08300, 2009.

[30] D. Du, J. S. X. Liu, G. Korn, and G. Mourou, "Laser-induced breakdown by impact ionization in si02 with pulse widths from 7 ns to 150 fs," *Appl. Phys. Lett.*, vol. 64, p. 3071, 1994.

[31] A. Couairon, L. Sudrie, M. Franco, B. Prade, and A. Mysyrowicz, "Filamentation and damage in fused silica induced by tightly focused femtosecond laser pulses," *Phys. Rev. B*, vol. 71, p. 125435, 2005.

[32] B. C. Stuart, M. D. Feit, S. Herman, A. M. Rubenchik, B. W. Shore, and M. D. Perry, "Nanosecond-to-femtosecond laser-induced breakdown in dielectrics," *Phys. Rev. B*, vol. 53, pp. 1749 - 1761, 1996.

[33] K. Tanimura, T. Tanaka, and N. Itoh, "Creation of quasistable lattice defects by electronic excitation in sio2," *Phys. Rev. Lett.*, vol. 51, pp. 423 - 426, 1983.

[34] C. Hnatovsky, R. S. Taylor, P. P. Rajeev, E. Simova, V. R. Bhardwaj, D. M. Rayner, and P. B. Corkum, "Pulse duration dependence of femtosecond-laser-fabricated nanogratings in fused silica," *Appl. Phys. Lett.*, vol. 87, p. 014104, 2005.

[35] R. W. Boyd, *Nonlinear Optics.* Academic Press, 1992.

[36] S. Grafström, "Photoassisted scanning tunneling microscopy," *J. Appl. Phys.*, vol. 91, pp. 1717–1753, 2002.

[37] V. R. Bhardwaj, E. Simova, P. P. Rajeev, C. Hnatovsky, R. S. Taylor, D. M. Rayner, and P. B. Corkum, "Optically produced arrays of planar nanostructures inside fused silica," *Phys. Rev. Lett.*, vol. 96, p. 057404, 2006.

[38] M. Gertsvolf, D. Grojo, H. Jean-Ruel, L. Ramunno, S. Lei, D. M. Rayner, and P. B. Corkum, "Self-organized defocusing micro-lenses created inside transparent dielectrics.," in *SPIE Photonics North 2008*, 2008.

[39] G. L. Yudin and M. Y. Ivanov, "Nonadiabatic tunnel ionization: Looking inside a laser cycle," *Phys. Rev. A*, vol. 64, p. 013409, 2001.

[40] M. Hentschel, R. Kienberger, C. Spielmann, G. A. Reider, N. Milosevic, T. Brabec, P. B. Corkum, U. Heinzmann, M. Drescher, and F. Krausz, "Attosecond metrology," *Nature*, vol. 414, pp. 509–513, 2001.

[41] M. Uiberacker, T. Uphues, M. Schultze, A. J. Verhoef, H. Kabachnik, V. N. M. andSchroder, M. Lezius, K. L. Kompa, H.-G. U. Kleineberg, U. Heinzmann, M. Drescher, and F. Krausz, "Attosecond real-time observation of electron tunnelling in atoms," *Nature*, vol. 446, p. 627, 2007.

[42] N. Dudovich, J. Levesque, O. Smirnova, D. Zeidler, D. Comtois, D. M. Ivanov, M.Yu.and Villeneuve, and P. B. Corkum, "Attosecond temporal gating with elliptically polarized light," *Phys. Rev. Lett*, vol. 97, p. 253903, 2006.

[43] F. Brunel, "Harmonic generation due to plasma effects in a gas undergoing multiphoton ionization in the high-intensity limit," *J. Opt. Soc. Am. B*, vol. 7, p. 521, 1990.

[44] D. E. Manolopoulos *J. Chem. Phys.*, vol. 117, p. 9552, 2002.

[45] W. Denk, J. H. Strickler, and W. W. Webb, "Two-photon laser scanning fluorescence microscopy," *Science*, vol. 248, pp. 73 – 76, April 1990.

[46] "www.crystallography.net."

[47] "www.jmol.com."

[48] C. Zener, "A theory of the electrical breakdown of solid dielectrics.," *Proc. Roy. Soc.*, vol. A145, p. 523, 1934.

[49] M. P. Marder, *Condensed Matter Physics.* Wiley, 2000.

[50] L. V. Keldysh, "Behavior of non-metallic crystals in strong electric fields," *JETP*, vol. 33, p. 994, 1957.

[51] X. Gonze, J. M. Beukena, R. Caracasa, F. Detrauxa, M. Fuchsa, G. M. Rignanesea, L. Sindica, M. Verstraetea, G. Zerahb, F. Jolletb, M. Torrentb, A. Royb, M. Mikamic, P. Ghosezd, R. J. Y., and D. C. Allane, "First-principles computation of material properties: the abinit software project," *Comput. Materials Science*, vol. 25, p. 478, 2002.

[52] X. Gonze, G. M. Rignanese, and R. Caracas, "First-principle studies of the lattice dynamics of crystals, and related properties," *Z. Kristallogr.*, vol. 220, p. 558, 2005.

[53] "www.abinit.org."

[54] N. Troullier and J. L. Martins *Phys. Rev. B*, vol. 43, p. 1993, 1991.

[55] J. P. Perdew, K. Burke, and M. Ernzerhof *Phys. Rev. Lett.*, vol. 77, p. 3865, 1996.

[56] S. M. Hankin, D. M. Villeneuve, P. B. Corkum, and D. M. Rayner, "Nonlinear ionization of organic molecules in high intensity laser fields," *Phys. Rev. Lett.*, vol. 84, pp. 5082–5085, May 2000.

[57] C. Pépin, D. Houde, H. Remita, T. Goulet, and J.-P. Jay-Gerin, "Evidence for resonance-enhanced multiphoton ionization of liquid water using 2 ev laser light: Variation of hydrated electron absorbance with

femtosecond pulse intensity," *Phys. Rev. Lett.*, vol. 69, pp. 3389–3392, Dec 1992.

[58] B. C. Stuart, M. D. Feit, A. M. Rubenchik, B. W. Shore, and M. D. Perry, "Laser-induced damage in dielectrics with nanosecond to subpicosecond pulses," *Phys. Rev. Lett.*, vol. 74, p. 22482251, 1995.

[59] A.-C. Tien, S. Backus, H. Kapteyn, M. Murnane, and G. Mourou, "Short-pulse laser damage in transparent materials as a function of pulse duration," *Phys. Rev. Lett.*, vol. 82, p. 38833886, 1999.

[60] Y. Shimotsuma, P. G. Kazansky, J. Qiu, and K. Hirao, "Self-organized nanogratings in glass irradiated by ultrashort light pulses," *Phys. Rev. Lett.*, vol. 91, p. 247405, 2003.

[61] A. Rosenfeld, M. Lorenz, R. Stoian, and D. Ashkenasi, "Ultrashort-laser-pulse damage threshold of transparent materials and the role of incubation," *Appl. Phys. A*, vol. 69, pp. S373 – S376, 1999.

[62] O. Efimov, S. Juodkazis, and H. Misawa, "Intrinsic single- and multiple-pulse laser-induced damage in silicate glasses in the femtosecond-to-nanosecond region," *Phys. Rev. A*, vol. 69, p. 042903, Apr 2004.

[63] C. B. Schaffer, A. Brodeur, and E. Mazur, "Laser-induced breakdown and damage in bulk transparent materials induced by tightly focused femtosecond laser pulses," *Meas. Sci. Technol.*, vol. 12, p. 17841794, 2001.

[64] A. Pasquarello and R. Car, "Identification of raman defect lines as signatures of ring structures in vitreous silica," *Phys. Rev. Lett.*, vol. 80, p. 51455147, 1998.

[65] J. W. Chan, T. Huser, S. Risbud, and D. M. Krol, "Structural changes in fused silica after exposure to focused femtosecond laser pulses," *Opt. Lett.*, vol. 26, pp. 1726–1728, NOV 1 2001.

[66] D. Homoelle, S. Wielandy, A. L. Gaeta, N. F. Borrelli, and C. Smith, "Infrared photosensitivity in silica glasses exposed to femtosecond laser pulses," *Opt. Lett.*, vol. 24, pp. 1311–1313, SEP 15 1999.

[67] K. Miura, J. R. Qiu, H. Inouye, T. Mitsuyu, and K. Hirao, "Photowritten optical waveguides in various glasses with ultrashort pulse laser," *Appl. Phys. Lett.*, vol. 71, pp. 3329–3331, DEC 8 1997.

[68] R. R. Gattass and E. Mazur, "Femtosecond laser micromachining in transparent materials," *Nature Photonics*, vol. 2, pp. 219–225, APR 2008.

[69] A. P. Joglekar, H. H. Liu, E. Meyhofer, G. Mourou, and A. J. Hunt, "Optics at critical intensity: Applications to nanomorphing," *PNAS*, vol. 101, pp. 5856–5861, APR 20 2004.

[70] E. Bricchi, B. G. Klappauf, and P. G. Kazansky, "Form birefringence and negative index change created by femtosecond direct writing in transparent materials," *Opt. Lett*, vol. 29, pp. 119–121, 2004.

[71] R. S. Taylor, C. Hnatovsky, E. Simova, P. P. Rajeev, D. M. Rayner, and P. B. Corkum, "Femtosecond laser erasing and rewriting of self-organized planar nanocracks in fused silica glass," *Opt. Lett.*, vol. 32, p. 2888, October 2007.

[72] C. Hnatovsky, R. S. Taylor, E. Simova, P. P. Rajeev, D. M. Rayner, V. R. Bhardwaj, and P. B. Corkum, "Fabrication of microchannels in glass using focused femtosecond laser radiation and selective chemical etching," *Appl. Phys. A*, 2006.

[73] M. Born and E. Wolf, *Principles of Optics.* Cambridge University Press, 1999.

[74] P. Corkum, D. M. Jonas, R. J. D. Miller, and A. M. Weiner, eds., *Polarization Dependence of Nanostructure Formation in Transparent Solids*, vol. 88 of *Springer Series in Chemical Physics*, Springer Berlin Heidelberg, 2007.

[75] R. S. Taylor, E. Simova, and C. Hnatovsky, "Creation of chiral structures inside fused silica glass," *Opt. Lett.*, vol. 33, pp. 1312–1314, 2008.

[76] G. D. Boyd and D. A. Kleinman, "Paramatric interaction of focused gaussian light beams," *J. Appl. Phys*, vol. 39, p. 3597, 1968.

[77] V. R. Bhardwaj, P. P. Rajeev, P. B. Corkum, and D. M. Rayner, "Strong field ionization inside transparent solids," *J. Phys. B*, vol. 39, p. S397S407, 2006.